Chapter 5
Cathode Materials with Two-Dimensional Structure

5.1 Introduction

For over 40 years, researchers have actively focused their works on the study of physicochemical properties of the so-called low-dimensional solids. Indeed these compounds find major applications in the conversion and storage of energy. Different steps in the progress in this field can be identified. DiSalvo in 1971, investigated the properties of transition-metal chalcogenides (TMCs) as intercalation complexes for advanced devices such as superconductors [1]. Broadhead invented, in July 1972, the first rechargeable nonaqueous battery in which the active material is incorporated in the layer structure; his patent suggests the use of TMCs such as TiS_2 and WS_2 [2]. Goodenough has established the ability of fast-ion conduction of certain metal oxides [3]; his discovery was soon followed by Japanese companies that commercialized the first lithium-ion batteries (LiBs). The lithium-ion technology has opened a wide research field both in physics and chemistry to find a class of materials for high voltage cells [1–3]. However, there remain several key materials issues such as the structural stability over several hundreds of cycles, which need to be solved. In the area of positive electrode materials, extensive investigations on the requirements of optimum-ideal electrode system have shown that transition-metal oxides, $A_xM_yO_n$ (A = Li, Na; M = Ni, Co, Mn, Cr, Fe) are the most promising systems with great potential for structural improvements for long cycle life.

This chapter provides the relationships between structural and electrochemical properties of lamellar compounds: the 3d-transition metal oxides currently studied as for their potential use in LiBs. First, we examine briefly three binary layered oxides, MoO_3, V_2O_5, and LiV_3O_8 which were proposed as intercalation compounds since at the end of 1970s. Then, the ternary layered oxides are considered. Starting from the historical and prototype compound $LiCoO_2$, which is the dominant positive electrode material employed by all Li-ion cell manufacturers so far, we state the broad family of layered oxides such as LiM_xO_y and their derivatives: the

metal-doped oxides $LiM_xM'_zO_y$, the solid-solutions LiM_xO_y-LiM'_xO_y and the composite materials such as the Li-rich oxides. For each class of materials, we review their electrochemical properties and discuss them as a function of the structural stability of the lattices. The surface modification (coating or encapsulation) of active particles that has led recently to encouraging results is also reviewed and discussed.

5.2   Binary Layered Oxides

5.2.1   MoO₃

The oxides and oxide-hydrates of molybdenum in its highest oxidation state display a variety of structural types involving linked MoO_6 octahedra. MoO_3 is such a host. Of the anhydrous MoO_3, the well-known orthorhombic form (α-MoO_3) is the stable form in normal conditions, which possesses a layered structure as shown in Fig. 5.1
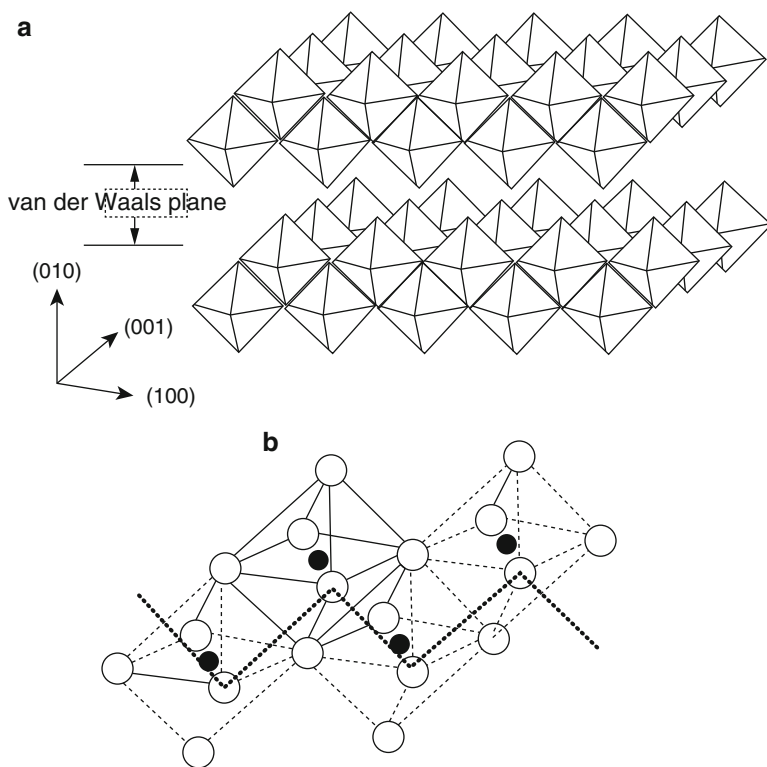
Fig. 5.1   (**a**) The layered structure at α-MoO_3 showing the interlayer van der Waals gap. (**b**) Detail of the Mo coordination
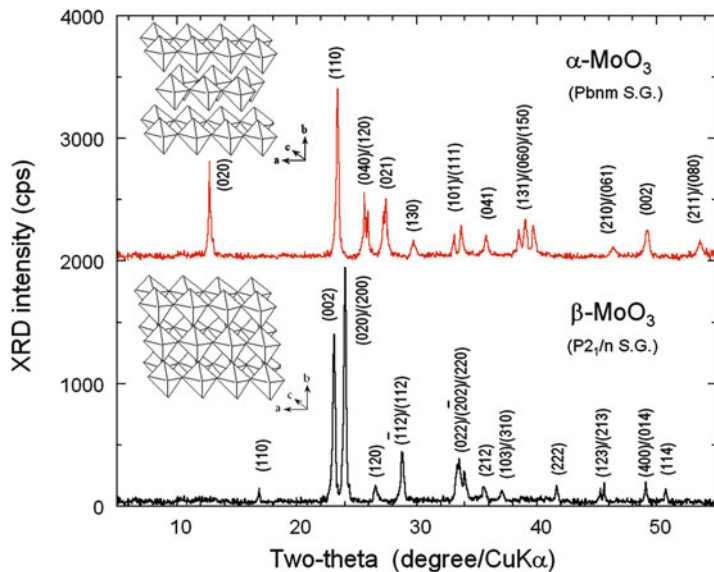
Fig. 5.2 XRD patterns of α-MoO₃ and β-MoO₃ crystals indexed in the monoclinic ($P2_1/n$ S.G.) and orthorhombic (*Pbnm* S.G.) system, respectively

[4] and three metastable phases: the β-MoO₃ phase which adopts the ReO₃-related structure, the MoO₃-II or ε-MoO₃ ($P2_1/m$ S.G.) metastable high pressure phase and the hexagonal MoO₃ form (h-MoO₃). Among the three stoichiometric solid hydrates of MoO₃ or "molybdic acids," white MoO₃·H₂O has a structure closely related to that of α-MoO₃ [5], consisting of isolated double chains of edge-sharing MoO₆ octahedra with each molybdenum atom bearing a coordinated water molecule.

Figure 5.2 shows the XRD patterns of α-MoO₃ and β-MoO₃ crystalline samples with the main features of the XRD patterns indexed in the orthorhombic (*Pbnm* S.G.) system with lattice parameters $a = 3.9621(4)$ Å, $b = 13.858(8)$ Å, $c = 3.972(1)$ Å and in the monoclinic ($P2_1/n$ S.G.) system with lattice parameters $a = 7.118(7)$ Å, $b = 5.379(2)$ Å, $c = 5.566(6)$ Å, $\beta = 91.87°$, respectively. Single crystals of α-MoO₃ have the shape of elongated platelets with the (010) axis perpendicular to the basal plane and the (001) axis along the longest edge. The orthorhombic structure was formed above 500 °C. The layered arrangement causes van der Waals interactions between parallel layers formed by MoO₆ octahedra that share edges in the (001) direction and are connected by corners in the (100) direction. The (0 k 0) intense Bragg lines suggest that this compound is a layered structure packed in the direction of the b-axis. The hexagonal MoO₃ is commonly synthesized using the chemical precipitation method and crystallizes with lattice parameters $a = 10.55$ Å and $c = 14.89$ Å ($P6_3/m$ S.G.).

Molybdenum oxides display a variety of structural types involving linked MoO_6 octahedra whose arrangements are favorable for intercalation process. Several studies have shown that Li^+ ions can be reversibly incorporated in Mo-O compounds [6–9]. The Li//α-MoO_3 system undergoes redox reactions with high reversibility, accommodating up to 1.5 Li per Mo atom and giving rise to a theoretical energy density of 745 Wh kg^{-1}, whereas the theoretical energy density of $MoO_{2.765}$ (~490 Wh kg^{-1}) is comparable to that of TiS_2. Despite the apparent diversity of the structural types shown by the Mo(VI) oxides and molybdenum-oxide hydrates, it is evident that they possess a number of common features in their reactions with lithium. Mo oxides offer high voltages and wide composition intervals accessible for lithium intercalation. The interest of α-MoO_3 arises from its layered structure presenting open channels for fast Li-ions diffusion, a higher electrochemical activity vs. Li^0/Li^+ than that of chalcogenides and the highest chemical stability among the oxide lattices [10].

The electrochemical lithium insertion into the MoO_3 framework can be described according the following reaction:

$$xLi^+ + xe^- + \left[Mo^{VI}\right]O_3 \leftrightarrows Li_x^+\left[Mo^{(6-x)+}\right]O_3, \tag{5.1}$$
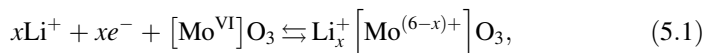
Assuming the reduction from Mo^{VI} to Mo^V and Mo^{IV} valence states, the maximum Li uptake occurs at $x = 1.5$. Figure 5.3 shows the discharge–charge curves of the Li//MoO_3 cell using anhydrous well-crystallized powders of the α-phase [11]. The electrochemical lithium insertion into the MoO_3 framework can be described assuming the reduction from Mo(VI) to Mo(V) and Mo(IV) oxidation states. The
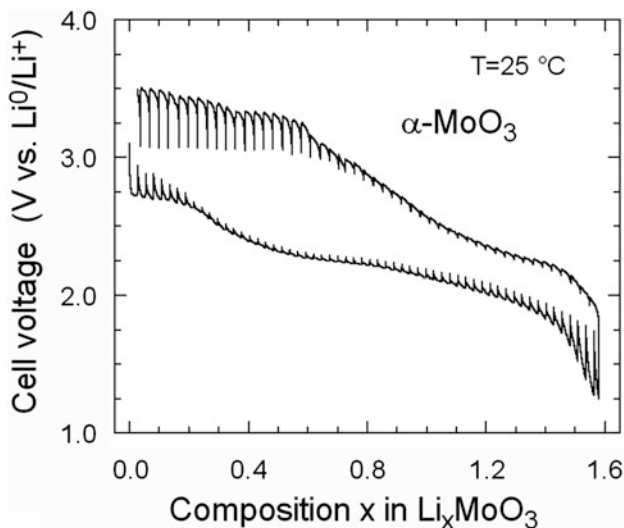

Fig. 5.3 Discharge–charge curves of the Li//MoO_3 cell using anhydrous well-crystallized powders of the α-phase. Reproduced with permission from [11]. Copyright 1997 Springer

capacity of MoO_3 observed here is approximately in agreement with the theoretical gravimetric capacity 280 mAh g^{-1}. α-MoO_3 is a very advantageous cathode material because it acts as a self-limiting voltage element at the end of the charge as reoxidation of Mo produces a resistive effect which induces a large polarization of the cell for potential of ≈3.5 V (Fig. 5.3).

Nadkarni and Simmons [12] studied the electrical properties of MoO_3 and reported that there is a donor band between the conduction and the valence bands due to oxygen vacancies. MoO_3 has the outer electron configuration $4s^5\ 5s^1$. If MoO_3 is considered to be ionic, i.e., composed only of Mo^{VI} and O^{2-} ions, the valence band would be composed of oxygen 2p states and the conduction band of empty 4d and 5s states [13]. Figure 5.4 shows the temperature dependence of the electrical conductivity of Li_xMoO_3 ($0.0 \le x \le 0.3$) intercalated by electrochemical titration. Upon Li intercalation the electrical conductivity of Li_xMoO_3 increases by two orders of magnitude and the temperature dependence of σ shows important changes in the conduction mechanism. The semiconducting character of MoO_3 gradually disappears and a degenerate semiconductor behavior is observed. For a degree of intercalation of $x = 0.3$, the material exhibits a metallic behavior. The metallic features are also observed in the temperature dependence of the Hall coefficient. This variation of mass is detected by the analysis of the absorption spectra near the plasma frequency. It is admitted that the mechanism for the conductivity of MoO_3 is the electron hopping between Mo^{6+} and Mo^{5+} sites. The increase of the conductivity with the addition of intercalants observed in Fig. 5.4 is linked to the diminution of the valence state of molybdenum ions by transfer of electrons from lithium to molybdenum. Further experiments are needed to elucidate the mechanism of the charge transfer occurring in transition-metal oxide compounds but the rigid-band model seems adequate in Li_xMoO_3 which found technological application in electrochromic rear mirror in automotive industry.

In MoO_3, electrical conductivity comes from the hopping of electrons forming small polarons between Mo^{6+} and Mo^{5+} ions. Infrared absorption studies of Li_xMoO_3 compounds revealed a transition small polaron to metallic features [14],
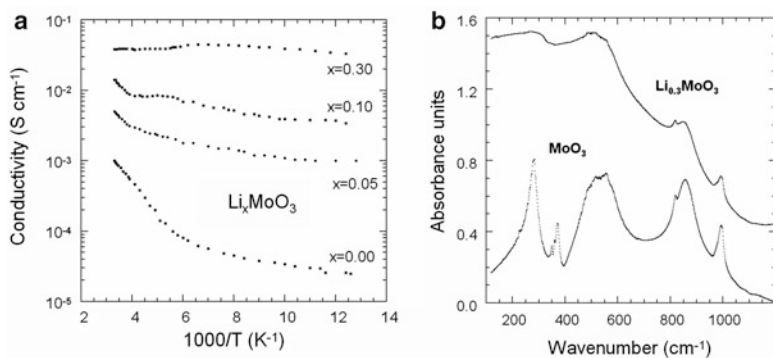
Fig. 5.4 (a) Arrhenius plot of the electrical conductivity of α-MoO_3 and Li_xMoO_3 and (b) FTIR absorption spectra of α-MoO_3 and $Li_{0.3}MoO_3$

in agreement with the analysis of the electrical conductivity. After intercalation the lattice vibration spectrum is completely screened by the free electrons in the host material. The Drude edge contribution, i.e., plasmon feature, is responsible for the metallic absorption due to high electron density in $Li_{0.3}MoO_3$ as shown in Fig. 5.4. The free-carrier absorption coefficient can be expressed by:

$$\alpha = \omega_p^2\, \tau \left[n\ c \left(1 + \omega^2 \tau^2 \right) \right], \tag{5.2}$$

where ω_p is the plasma frequency, τ is the relaxation time of the free carrier, n is the refractive index, and c is the light velocity. Using Eq. (5.2), the fit of experimental data gives a carrier concentration of 5×10^{16} cm^{-3} in $Li_{0.3}MoO_3$. This value is in good agreement with the Hall measurements. In MoO_3, the bonding framework is composed of five $O(p_\pi)$ and three $Mo(t_{2g})$ orbitals, which interact to form π and π^* bands [5]. As the extra electrons supplied by the inserted lithium are in the antibonding π^* states, $Li_{0.3}MoO_3$ is expected to exhibit a two-dimensional type of electronic conductivity. The narrowing of the conduction band leads to an increase in the effective electron mass which affects the position of the Drude edge in Li_xMoO_3 phases. The temperature dependence of the absorption coefficient shows a small increase of α with temperature, which can be attributed to the fact that Li-intercalated MoO_3 is a degenerate semiconductor for $x = 0.3$.

5.2.2 V_2O_5

Vanadium pentoxide, V_2O_5, was one of the earliest studied ICs that can exhibit several different phases upon intercalation of 3Li per formula. V_2O_5 crystallizes with an orthorhombic unit cell structure and belongs to the *Pmnm* space group with lattice parameters $a = 11.510$ Å, $b = 3.563$ Å, and $c = 4.369$ Å [15, 16]. The crystal structure of orthorhombic V_2O_5 is usually described as made up of chains of edge-sharing VO_5 square pyramids (Fig. 5.5a). These chains are linked together via corner sharing. The distorted polyhedra have a short vanadyl bond (1.54 Å) and four oxygen atoms located in the basal plane at distances ranging from 1.78 to 2.02 Å (Fig. 5.5b). Here, the oxygen atoms surrounding a vanadium atom are geometrically labelled O_1, O_{21}, O_{23}, O'_{23}, and O_3, respectively. In the deformed octahedron including the O'_1 atom, a V–O_1 bond length is the shortest: 1.54 Å, and a V–O'_1 distance is 2.81 Å. The deformed octahedrons, which have common corners in the b direction are linked by common edges, giving rise to chains in the a-direction.

   The complex phase diagram of lithia-vanadium pentoxide had been described by several groups [17–19] employing electrochemical and chemical synthesis. Figure 5.6 shows a schematic representation of the α- and γ-$Li_xV_2O_5$ structure and the Li-V_2O_5 phase diagram proposed by Galy [20]. The discharge curve of a Li// $Li_xV_2O_5$ cell in the range $0 \leq x \leq 3$ is shown in Fig. 5.7. It is seen that insertion of up to 1 Li per formula unit proceeds in two distinct steps, each accounting for
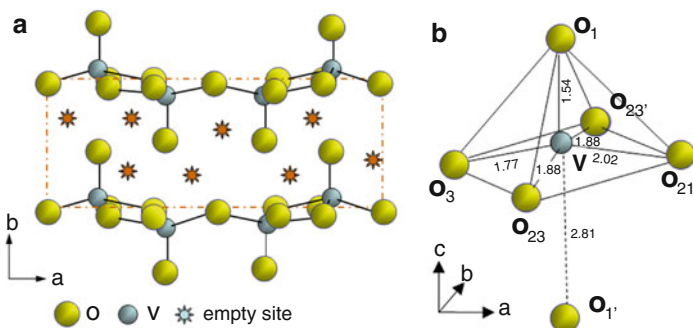
Fig. 5.5 (**a**) Projection of the layered structure of V_2O_5 on (001). Superimposed oxygen atoms are symmetrically displaced. (**b**) The deformed pyramid of the V_2O_5 structure, shown with the coordinate system and labels of V, O_1, O_{21}, O_{23}, and O_3 atoms. The *solid* and *dashed lines* schematically represent the chemical bonds, and numerical values indicate the bonding length (Å) between atoms. The O'_1 atom is the O_1 type atom belonging to the neighbor pyramid painting at opposite direction
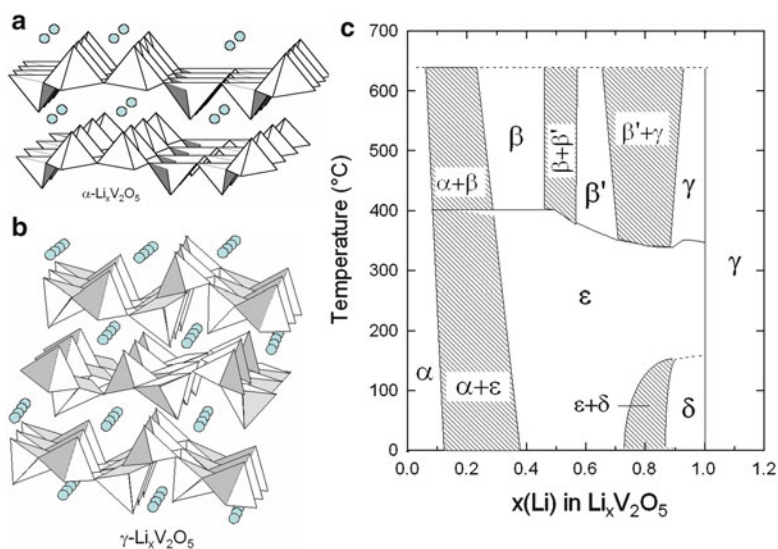
Fig. 5.6 Schematic representation of (**a**) α-$Li_xV_2O_5$, (**b**) γ-$Li_xV_2O_5$, and (**c**) the Li-V_2O_5 phase diagram

half the charge. Upon lithium intercalation up to $x = 3$ in $Li_xV_2O_5$, a series a structural rearrangement (α-, ε-, δ-, and γ-$Li_xV_2O_5$ phases) emerges that corresponds to a theoretical specific capacity of 442 mAh g^{-1}.

When the amount of lithium content is increased beyond $x = 1$, the discharge curve exhibits a sharp potential drop followed by a region with a plateau characteristic of a two-phase domain, for which the δ- and γ-$Li_xV_2O_5$ phases are in
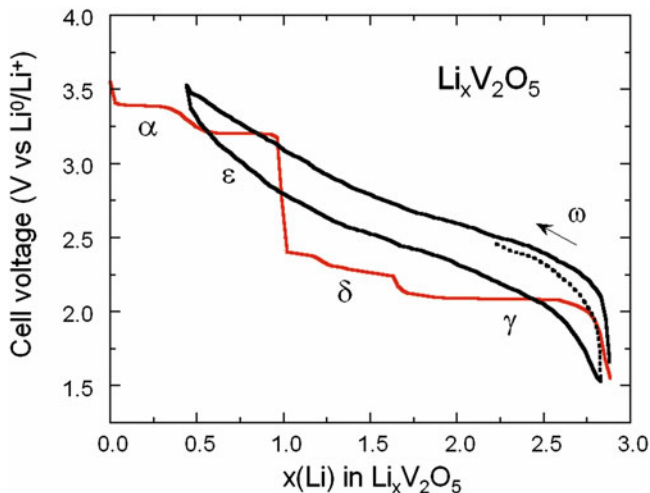
**Fig. 5.7** Discharge curve of the $Li//Li_xV_2O_5$ electrochemical cell. At $x = 3$, the system reaches the NaCl-like ω-$Li_{3-x}V_2O_5$ phase (*black curve*)

equilibrium. When the amount of lithium inserted is restricted to $x < 2$, the reversibility in the composition range $0 < x < 1$ is not much affected [21]. At $x \approx 3$, the new ω-V_2O_5 phase appears [22, 23]. This phase has a NaCl-like structure with high number of vacancies. In shear vanadium oxide, V_2O_5, the O^{2-} along the shear planes are bonded to three cations and, indeed, high values of the chemical diffusion coefficient have been measured. $Li_xV_2O_5$ shows values of 10^{-8} cm^2 s^{-1} in the range 0.01–0.98 [24]. Recently, Li et al. [25] reported the lithium insertion in the β-$Li_xV_2O_5$ phases ($0 < x \leq 3$) for powders synthesized by the hydrothermal treatment of α-V_2O_5 at 220 °C for 24 h followed by post-heating at 650 °C for 3 h. The rigid 3D host lattice of the monoclinic tunnel-like β-V_2O_5 shows desirable reversibility upon 3Li uptake per formula unit and a discharge capacity exceeding 330 mAh g^{-1} at current density 10 mA g^{-1} in the potential range 4.0–1.8 V.

5.2.3 LiV$_3$O$_8$

Lithium trivanadate, LiV_3O_8, is a mixed-valence oxide. Firstly reported by Wadsley [26], LiV_3O_8 is a quasi-layered compound, which can be regarded as a lithia-stabilized V_2O_5 compound. It crystallizes in a monoclinic symmetry ($P2_1/m$ S.G.) and consists of octahedral (VO$_6$) octahedral and trigonal bipyramidal (VO$_5$) ribbons. In this structure, distorted (VO$_6$) octahedra are connected by shared edges and vertices to form (V$_3$O$_8$)$^-$ anions that stack one upon another to form quasi layers (Fig. 5.8). The spacing between slabs is sufficiently flexible to accommodate guest species on octahedral and tetrahedral interstitial sites [27, 28].
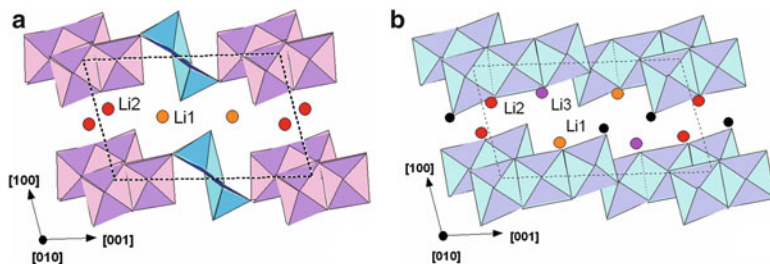
Fig. 5.8 (**a**) Representation of [010] view of the layered structure of LiV_3O_8 ($P2_1/m$ S.G.). The *circles* represent the octahedral site $Li(1)$ and the tetrahedral site $Li(2)$ between the layers. (**b**) [010] View of the structure of $Li_4V_3O_8$. The c-axis is horizontal within a V_3O_8 layer

Fig. 5.9 The typical voltage vs. composition $x(Li)$ curve for $Li//LiV_3O_8$ cell. The discharge–charge processes is rather complex reactions that correspond to multistep Li insertion–extraction associated with the reduction–oxidation of vanadium ions. The different steps are indicated
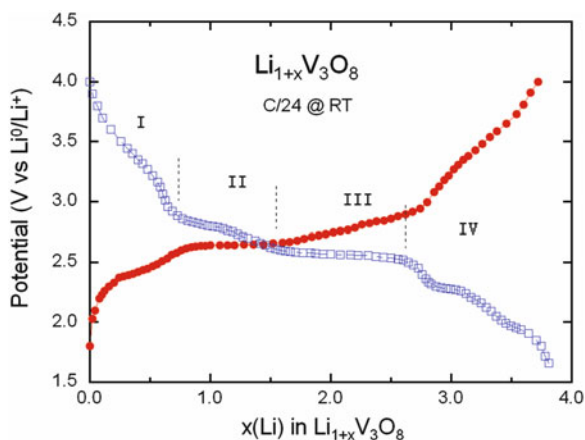

When intercalating Li^+ ions into the LiV_3O_8 framework to the composition of $Li_4V_3O_8$, the V_3O_8 framework remains intact and the monoclinic unit cell parameters vary isotropically with phase changes [29]. As reported by several workers [28, 30–34], the V_3O_8 sublattice is very stable upon lithiation leading to composition $Li_{3.8}V_3O_8$ owing to the availability of the 2D interstitial space for the transport of Li^+ ions. This feature makes LiV_3O_8 an attractive cathode candidate for lithium secondary batteries with a specific capacity higher than 300 mAh g^{-1}. Electrochemical intercalation mechanism was investigated including long-term cycling and kinetics Li^+ ions [35–37]. LiV_3O_8 has a lower Li-ion diffusion coefficient ($\sim 10^{-13}$ cm^2 s^{-1}) than $Li_xV_2O_5$ ($\sim 10^{-10}$ cm^2 s^{-1}) [37]. Jouanneau et al. [38] reported that the dissolution of a small quantity of V^{III} in the electrolyte occurring during the reduction at 2.3 V depends on the morphology of the powders. Figure 5.9 shows the typical voltage vs. composition $x(Li)$ curve for $Li//Li_{1.2+x}V_3O_8$ cell. Initial discharge capacity of 308 mAh g^{-1} at 20 mA g^{-1} corresponds at $x = 3.8$Li uptake. The discharge curve shows a rather complex process, at first the open circuit voltage of $Li_{1.2+x}V_3O_8$ drops rapidly to 2.85 V for the composition $x \leq 0.8$ (S-shape region), where the lithium is

inserted into the interstitial sites Li(2). Then, the voltage drops less rapidly from 2.85 to 2.7 V in the domain $0.8 \leq x \leq 1.7$, where the lithium is inserted into the interstitial space of the $Li_2V_3O_8$ structure, possibly in the $S_t(1)$ and $S_t(2)$ tetrahedral sites. At $x > 1.7$, the voltage curve shows a plateau at 2.5 V characteristics of a two-phase system, with the coexistence of $Li_{2.9}V_3O_8$ compound and the defect rock-salt structure of nominal composition $Li_4V_3O_8$. $Li_{1+\delta}V_3O_8$ is a semiconductor that exhibits a polaronic conduction ($\sigma_e = 10^{-5}$ S cm^{-1} at room temperature, $E_a = 0.25$ eV).

As for all ICs, the method of preparation of LiV_3O_8 appears to be important to its electrochemical features. Synthesis technique include: the traditional solid-state reaction using Li_2VO_3 and V_2O_5 at high temperature (680 °C) [38], sol–gel method [39], precipitation technique [40], hydrothermal method [41], freeze-drying technique [42], combustion synthesis [43], spray pyrolysis route [44] and polymer assisted method [45]. West et al. [32] have compared the capacity and cycling behavior of several samples. Nanostructured LiV_3O_8 cathode materials were synthesized under several forms including nanocrystals [46, 47], nanowires [48, 49], nanorods [41, 50], and nanoflakes [51]. Improvement of the intercalation process was also achieved by effective doping [52]. Nanosheets with a thickness of 15–30 nm width were synthesized by hydrothermal method combined with a solid-state process using uniform $(NH_4)_{0.5}V_2O_5$ nanosheets as the precursor. Good cycling stability of 149 mAh g^{-1} at $5C$ was demonstrated by the stability retention of 85 % [53]. Surface modification with conducting materials appears to be efficient to enhance the electrochemical properties of LiV_3O_8 via suppressing the dissolution of active materials and the overall phase change [54]. Kumagai et al. [55] reported the use of LiV_3O_8 powders ultrasonically treated.

5.3 Ternary Layered Oxides

This class of materials include the $LiMO_2$ compounds ($M =$ Co, Ni, Cr) and the related oxides $LiCoM'O_2$ where M' is a substituting trivalent or divalent element ($M' =$ Ni, Cr, Fe, Al, B, Mg, etc.). $LiMO_2$ oxides adopt the α-$NaFeO_2$-type crystallographic structure that belongs to $R\overline{3}m$ (D_{3d}^5) space group. This structure derives from the NaCl structure with a stacking of Li ions between adjacent MO_2 slabs [56]. The individual coordination octahedron is face-sharing. They show higher operating voltage than the conventional 3-V systems; a relationship between the level of operating voltage of transition-metal oxides and their d-electron character has been recognized. Among them, $LiNiO_2$ and $LiCoO_2$, as well as their solid solutions $LiN_{1-y}Co_yO_2$, are isostructural with α-$NaFeO_2$. Crystal radius for Co^{3+} ion (68 pm) is almost the same as that of Ni^{3+} ion (70 pm) (ions in octahedral sites in the low-spin state), so that a solid solution of $LiNiO_2$ and $LiCoO_2$ may be obtained [57]. Schematic crystal structures of P2-, P3-, O2-, and O3-$LiMO_2$ are shown in Fig. 5.10. The labels "O2" and "O3" indicate that the Li environment is octahedral in both cases, but the stacking sequences of the oxygen layers are $ABCB$ and $ABCABC$, leading to two and three sets of Co and Li layers in the hexagonal unit
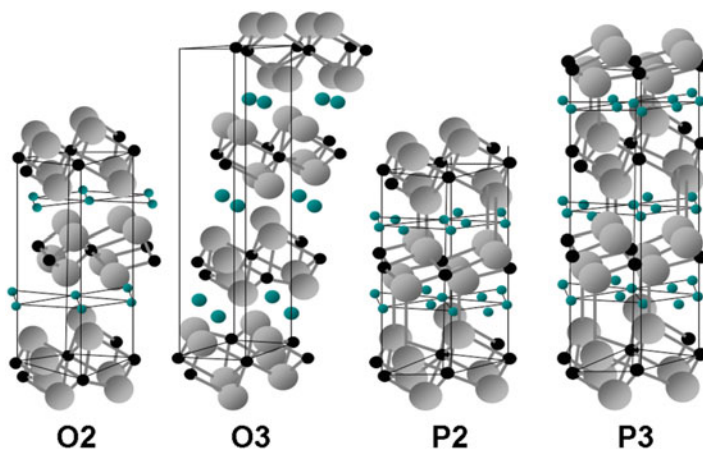
Fig. 5.10 Crystal structures of P2-, P3-, O2-, and O3-type LiMO_2. Here O states for octahedral coordination of the cation and the number corresponds to the number of layers building the unit cell. In O3-type each layer is related to the others by translation whereas in O2-type every second layer is rotated by 60°

cell, respectively. The electrochemical performance of O2-LiCoO$_2$ is competitive to that of conventional O3-LiCoO$_2$, but its synthesis is more difficult and it is thus not convenient for industrial application [58].

Studies of structural properties of the α-NaFeO$_2$ type structure have shown that the oxygen sublattice can be considered as distorted from the *fcc* array in the direction of the hexagonal *c* axis [59, 60]. Considering the XRD patterns, the trigonal distortion gives rise to a splitting of the (006, 102) and (108, 110) Bragg lines that are characteristic of the lamellar framework. When the distortion in the *c* direction is absent, the ratio of the lattice parameters, *c/a* is √24 (4.899), and the (006, 102) and (108, 110) lines will merge into single peaks [61].

5.3.1 LiCoO$_2$ (LCO)

Identified and tested by Goodenough et al. [3, 62] LiCoO$_2$ (LCO) is considered as the prototypal cathode oxide in which fast charge–discharge reaction occurs in the potential range 3.6–4.2 V [63]. After almost three decades, this material and its derivatives were still used in commercial lithium-ion batteries in the form of "normal" thermodynamically stable O3-structure as well as in the O2-structure. In the O3-LiCoO$_2$ lattice, *M* cations are located in octahedral 3*a* (000) sites and oxygen anions are in a cubic close-packing (*ccp*), occupying the 6*c* (00*z*, 000*z*) sites. Li ions reside at Wyckoff 3*b* (00½) sites. The transition-metal and lithium ions are occupying the alternating (111) planes. The Bravais cell contains one molecule (*Z* = 1). The lattice constants (*a* = 2.806 Å, *c* = 9.52 Å) show that

O2-LiCoO$_2$ has a slightly larger interlayer spacing than the conventional O3-LiCoO$_2$ lattice ($a = 2.816$ Å, $c = 14.08$ Å). This former material has a more pronounced layered structure. For the refinement of the O2-LiCoO$_2$ lattice, the $P6_3mc$ (no. 186) space group was used with oxygen and cobalt atoms located on $2a$ and $2b$ sites, respectively. The strong covalent bond in LiCoO$_2$, with reduced Co–O bond distance, results in stabilization of Co^{3+} in low-spin ground state that is $d^6 = (t_{2g})^6(e_g)^0$, $S = 0$, and reduces the electronic conductivity of the compound.

A wide range of techniques were used to prepare LCO with different characteristics: morphology, size (from micron to nanometer), and size distribution of grains, all important factors in the development of efficient cathode materials. In the synthesis of LCO, the rhombohedral structure is obtained at high temperature $T > 850$ °C (called HT-LCO), while a low temperature phase (LT-LCO) was prepared around 400 °C with a spinel structure Li$_2$Co$_2$O$_4$ [64]. Shao-Horn et al. [65] found that LT-LCO nucleates from an intermediate Li$_x$Co$_{1-x}$[Co$_2$]O$_4$ spinel product before transforming more slowly to HT-LCO.

The traditional solid-state process is very popular [56, 66, 67]. It consists in sintering the mixture of cobalt carbonate (or oxide) and lithium carbonate (or hydroxide) at high temperature $T \approx 850$–900 °C in air for several hours. Numerous other techniques of LCO preparation, aiming to obtain fine grains with narrower size distribution, include: sol–gel method using various chelating agents [68, 69], combustion synthesis [70], molten salt synthesis [71], mechanical activation [72], freeze-dried salt synthesis [73], hydrothermal route [74], and microwave synthesis [75]. Akimoto et al. [76] succeeded to grow LiCoO$_2$ single-crystal by a flux method of the slow cooling from 900 °C in a gold crucible.

In Fig. 5.11a, the charge–discharge characteristics of the Li//LiCoO$_2$ cell is reported with the various phase in Li$_x$CoO$_2$ in the range $0 < x < 1$ [67, 77]. In the
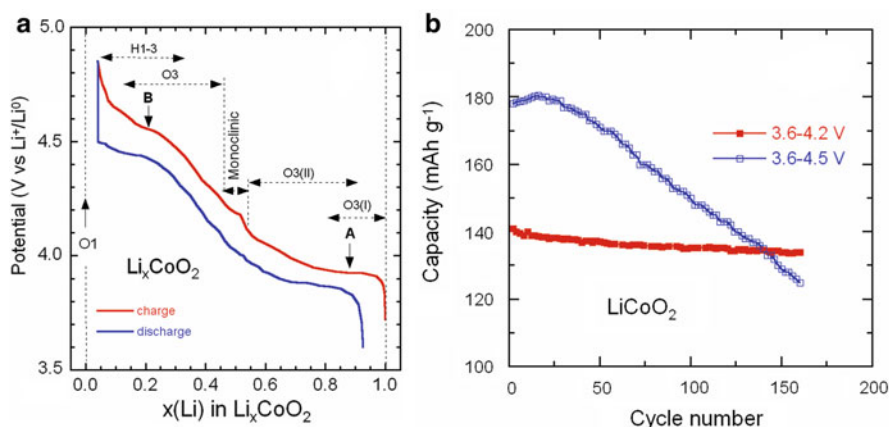
Fig. 5.11 (**a**) Electrochemical features of the Li//LiCoO$_2$ cycled in the voltage range 3.0–4.8 V. Powders were synthesized by sol–gel method. (**b**) Capacity retention as a function of the working region. When the LiCoO$_2$ electrode is operating with the cutoff voltage 3.6–4.5 V, the capacity fading becomes very important

potential domain 2.5–4.3 V, the voltage profile of $LiCoO_2$ displays the typical plateau at ca. 3.92 V, which is the characteristic feature of the first phase transition denoted H1 $\leftrightarrow$ H2. This transition has been associated to a semiconductor-metal transition. The capacity retention of $LiCoO_2$ electrode is clearly depicted as a function of the working region. For a cell working between 3.6 and 4.2 V, the capacity is quite stable, while for a voltage cutoff 3.6–4.5 V the capacity decreases drastically with the cycle number due to the loss of oxygen at deep lithium extraction (Fig. 5.11b). The tendency to lose oxygen at lower lithium contents appears to limit the practical capacity of the Li//$LiCoO_2$ system to 140 mAh g^{-1}. Both O2-LCO and O3-LCO materials exhibit similar reversible phase transition as a function of the x(Li) [78, 79]. The first transition (at 3.90 V for O3 and 3.73 V for O2) is connected with a large change in lattice constant but minor change in crystal structure; this modification is noted H1 $\leftrightarrow$ H2 in O3-$LiCoO_2$ and $O2_1 \leftrightarrow O2_2$ in O2-$LiCoO_2$. When Li_xCoO_2 approaches $x = 0.5$, both materials exhibit a phase transition that possibly is due to lithium ordering. This is a continuous phase transition (H2 $\leftrightarrow$ M) to the monoclinic phase in O3. If more Li is removed, another continuous transition M $\leftrightarrow$ H3 occurs in O3-$LiCoO_2$. However, there are some controversies on the crystal chemistry and the phase diagram of delithiated Li_xCoO_2 [80].

The structural evolution of the $LiCoO_2$ phase during Li extraction (charge process) is still subject to debate (Fig. 5.12). Structural and chemical stabilities of $Li_{1-x}CoO_{2-\delta}$ and $Li_{1-x}Ni_{0.85}Co_{0.15}O_{2-\delta}$ with $0 \leq (1-x) \leq 1$ electrode materials have been investigated by chemically extracting lithium using acetonitrile solution of NO_2BF_4 [81]. This technique has the advantage of using samples free of carbon and binder. The $Li_xCoO_{2-\delta}$ and $Li_{1-x}Ni_{0.85}Co_{0.15}O_{2-\delta}$ systems maintain the initial O3-type structure, for $0.5 \leq x \leq 1$ and $0.3 \leq x \leq 1$, respectively. While $Li_xCoO_{2-\delta}$ begins to form a P3-type phase for $x < 0.5$, $Li_{1-x}Ni_{0.85}Co_{0.15}O_{2-\delta}$ begins to form a new O3-type phase, designated as O3′ phase, for $x < 0.3$. The P3-type and the O3′ phases have smaller c parameters than do the O3-type phase and oxygen contents lower than 2, resulting in a loss of oxygen from the lattice for $x < 0.5$ and $x < 0.3$, respectively, for $Li_xCoO_{2-\delta}$ and $Li_xNi_{0.85}Co_{0.15}O_{2-\delta}$. The formation of the P3-type and O3′ phase is related to the introduction of holes into the O:$2p$ band and the O–O interaction. The loss of oxygen was also confirmed for electrochemically charged samples. Unfortunately, only 50 % of the theoretical capacity of $LiCoO_2$ could be practically utilized. This corresponds to a reversible extraction/insertion of 0.5 Li per cobalt and a practical capacity of 140 mAh g^{-1} because capacity fade occurs below $x < 0.5$ in Li_xCoO_2. Reimers et al. [82] attributed the limitation in practical capacity to an ordering of lithium ions and consequent structural distortions around $x = 0.5$ in Li_xCoO_2. However, Chebiam et al. [78] believed that the limited capacity could be due to chemical instability of Li_xCoO_2 at deep charge with $x < 0.5$. One way to overcome the chemical instability of $Li_xCoO_{2-\delta}$ could be the modification of its surface with nanophase inert oxides such as Al_2O_3 and ZrO_2 [83]. A set of experiments, XRD, photoelectron spectroscopy and band structure calculations, shows that the degradation and fatigue of Li_xCoO_2 and Li_xNiO_2 ($0.5 < x < 1$) are due to the broadening of the Co/Ni $3d$ states upon Li deintercalation [84].
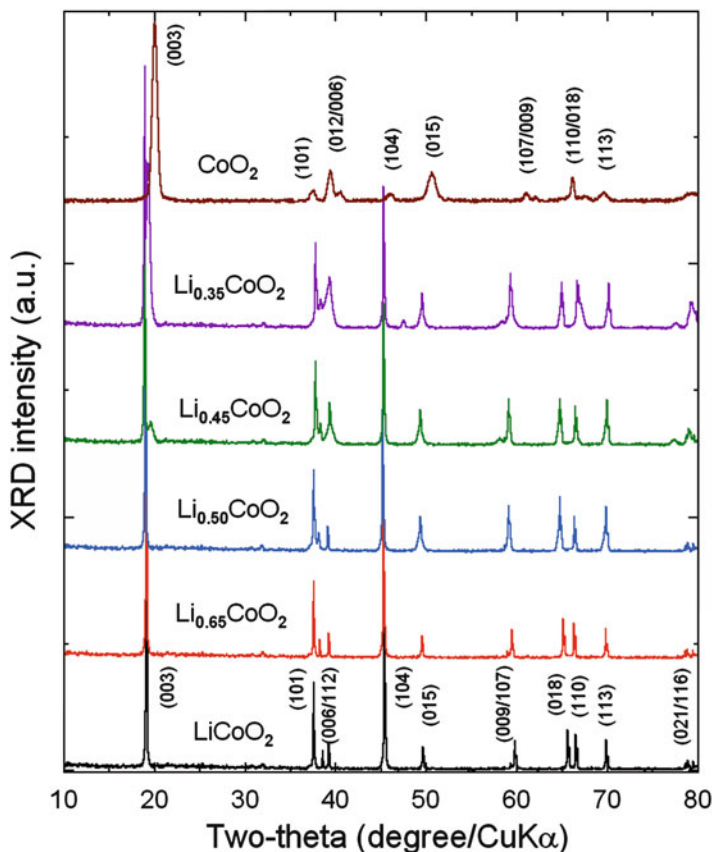
Fig. 5.12 XRD patterns of LiCoO$_2$ and chemically delithiated using with a required amount of the NO$_2$BF$_4$ oxidizing agent and anhydrous acetonitrile mixture. Note that the (003) reflection of the end member CoO$_2$-d occurs at a slightly higher $2q$ value than that of the new phase formed at x = 0.45, which could be due to a small lithium solid solubility range for the P3-type phase and/or changes in the oxygen content of the P3-type phase with the overall lithium content

5.3.2 LiNiO$_2$ (LNO)

LiNiO$_2$ (LNO) is isostructural with LiCoO$_2$ and has the O3 layer structure. The Ni$^{3+/4+}$ couple with a high lithium chemical potential $\mu_{Li(c)}$ provides a high cell voltage of around 4 V (Fig. 5.13) like LiCoO$_2$. However, LiNiO$_2$ suffers from a few drawbacks: (1) the difficulty to synthesize LiNiO$_2$ with all the nickel ions in the Ni^{3+} valence state and crystallized in a perfectly ordered phase without a mixing of cations Li$^+$ and Ni^{2+} ions in the insterslab space to form the [Li$_{1-x}$Ni$_x$]$_{3b}$[Ni]$_{3a}$O$_2$, where 3a and 3b are the site occupancy into the intra- and inter-layer space, respectively [85], (2) the Jahn–Teller distortion (tetragonal structural distortion) associated with the low spin Ni^{3+}:d^7 ($t_{2g}{}^6e_g{}^1$) ion [86], (3) irreversible phase transitions occurring during the charge–discharge process [87], and (4) exothermic
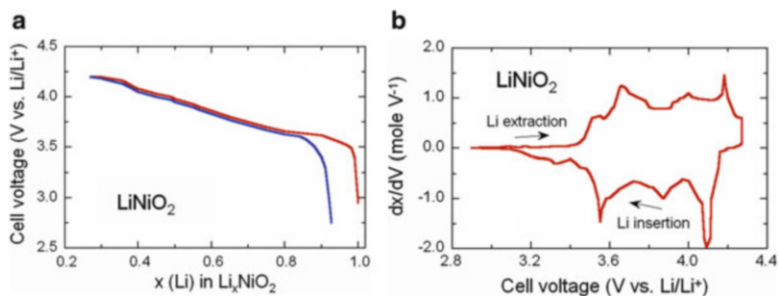
Fig. 5.13 Electrochemical features of LiNiO$_2$ powders: (**a**) first charge-discharge profile and (**b**) the incremental capacity

Fig. 5.14 The charge discharge profile of aluminum doped LiNi$_{1-y}$Al$_y$O$_2$ with y $=0.05$
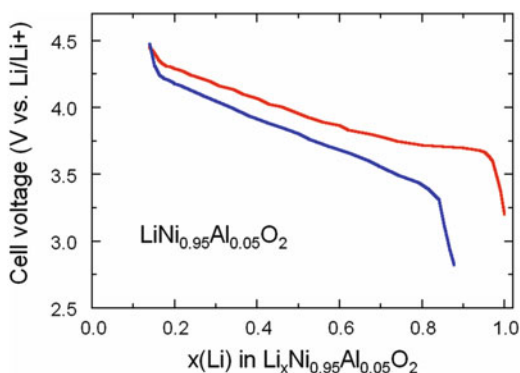
release of oxygen at elevated temperatures and safety concerns in the charged state [88]. The deviation of Li$_{1-x}$Ni$_{1+x}$O$_2$ from stoichiometry was studied by magnetic measurements [89]. We return to the magnetic properties of this material in Chap. 13 devoted to experimental technics.

As a result, pure LiNiO$_2$ is not a promising material for commercial lithium-ion cells although nickel is slightly less expensive and less toxic than cobalt. The formation of low lithium content Li$_x$NiO$_2$ ($x < 0.2$) causes cycle life failure. In addition, the material becomes highly catalytic toward electrolyte oxidation and some of the nickel ions may migrate to lithium sites. LNO is considered as thermally unstable in its charged state [90]. The formation of pure LNO is difficult, and residual Ni^{II} (up to 1–2 %) exist between the NiO$_6$ slabs. In fact, the irreversibility during the first cycle of charge–discharge is mainly related to the amount of Ni^{II} between the slabs, which require extra charge for oxidation to higher valency state [91], when electrolyte decomposition is controlled. Through careful synthesis and adjustment of lithium concentration in the material during heat treatment, it was obtained LNO very close to stoichiometry. In order to stabilize the structure of LiNiO$_2$ at low lithium content, sp elements such as B and Al were used as dopant of the LNO materials. These doping elements do not participate in oxidation reduction processes during charge–discharge of the cell. Figure 5.14 shows the

charge–discharge of aluminum doped $LiNi_{1-y}Al_yO_2$ with $y = 0.05$. The specific capacity of the cell reduces as a function of Al content, as the Al does not participate in the redox process. The capacity changes almost linearly with respect to the Al content up to 25 at%. This result may indicate a solubility limit in the formation of a solid solution between $LiAlO_2$ and $LiNiO_2$. It is also observed that the first charge–discharge irreversibility also increases as the amounts of Al in the samples were increased. The extra nickel in the lithium sites may cause the increase in first cycle irreversibility [92]. Ohzuku et al. [93] suggested the composition $LiNi_{3/4}Al_{1/5}O_2$ as more stable compound for lithium-ion batteries.

5.3.3 $LiNi_{1-y}Co_yO_2$ (NCO)

Efforts are currently done to improve the electrochemical performance of electrodes based on $LiNiO_2$ oxides, by forming the $LiNi_{1-y}Co_yO_2$ (NCO) solid solutions that are considered as Ni-rich compounds. Delmas et al. [94] pioneered studies of the NCO system. These solid solutions lead to successful results and progress has already been made to overcome the capacity fading by doping with several cations; it was noticed that the cationic mixing in the lithium sites still remains but at lower extent [95–99]. Many techniques were utilized for the NCO preparation. Julien et al. [100] synthesized $LiNi_{0.3}Co_{0.7}O_2$ powders of 510 nm particle size by the glycine–nitrate combustion process. This sample had significantly higher capacity (140 mAh g^{-1}) than samples synthesized by the sol–gel method (125 mAh g^{-1}). Julien et al. [69] prepared NCO by sol–gel technique assisted by citric acid as chelating agent. The structural properties of NCOs are found to be similar to their parent oxide, O3-$LiCoO_2$. A slight increase of the $(Co,Ni)O_2$ slab covalency is observed in $LiNi_{1-y}Co_yO_2$ powders. FTIR absorption spectra indicate the slight modification in the local structure related to the short-range environment of oxygen coordination around the cations in oxide lattices [101]. The variation of the lattice parameters as a function of the substitution of Co for Ni in $LiNi_{1-y}Co_yO_2$ reported in Fig. 5.15 These graphs follow the Vegard's law showing that the solid-solution is completed in these compounds. An interesting point to emphasize is the variation of the (c/a) ratio, which characterizes the degree of anisotropy of the layered structure. This criterion establishes the deviation from the hexagonal-close-packed structure when $(c/a) > 4.92$ for $y = 0$ and $(c/a) < 4.99$ for $y = 1$ [97]. Such graphs are also plotted in Fig. 5.15 for $LiNi_{1-y}Co_yO_2$ synthesized by wet chemistry via citrate route. From the plot (c/a) vs. y, we can appreciate the cation mixing effect. The binding energy of the Co–O bond being higher than that of the Ni–O bond, the strong Co–O skeleton can contribute to the stability of $LiNi_{1-y}Co_yO_2$ in the charged state.

In the case of $LiNi_{1-y}Co_yO_2$, even a small cobalt content shows the effect of reducing the amount of Ni^{3+} present in the $3a$ sites, stabilizing the layered structure and enhancing electrochemical capacity and the reversibility of the charge–discharge process. The same effect may occur when iron is partially
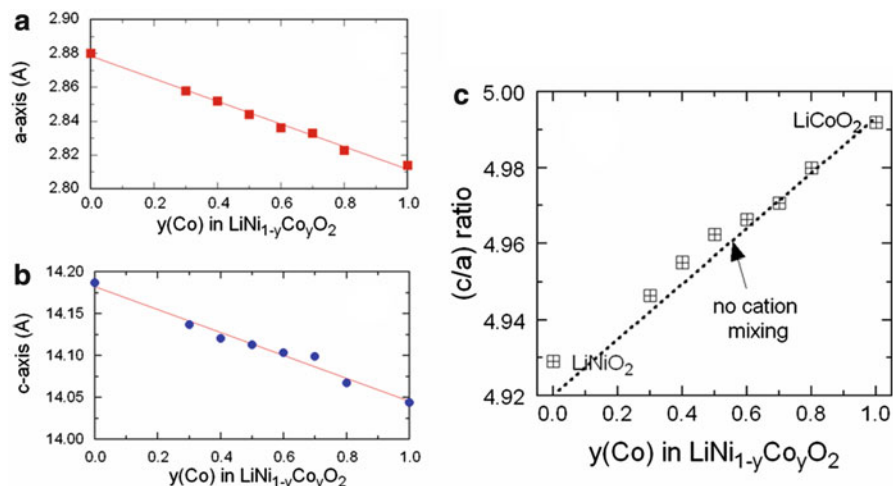
Fig. 5.15 (**a**) and (**b**) The variation of hexagonal unit-cell parameters with cobalt concentration y in $LiCo_yNi_{1-y}O_2$ solid solution. (**c**) The variation of the (c/a) ratio as a function of cobalt content. *Dashed line* represents the (c/a) vs. y relationship without cation mixing effect

substituted for cobalt in $LiFeO_2$: the layered structure is thought to be stabilized by cobalt ions present, reducing the amount of Fe^{3+} present in the $3a$ sites, thus facilitating lithium diffusion and rendering lithium deintercalation possible. The cathode layered structure enables fast 2D Li^+-ion diffusion and direct metal–metal intercation across the shared octahedral edges, which supports high operating voltage (>4.0 V vs. Li^0/Li^+). As experimental facts, the iron-enrichment on the cathode surface of $LiNi_{1-y}Fe_yO_2$ and $LiCo_{1-y}Fe_yO_2$ prevents surface-electrolyte instability at these high operating voltages and Fe-substituted cathodes exhibit superior rate capability and lower surface resistance (R_s) and charge transfer resistance (R_{ct}) compared to the unsubstituted cathode. In $LiNi_{1-y}Fe_yO_2$, Li sites are reportedly Ni and Fe, and their oxidation states are 2+ and 3+, respectively and Fe^{3+} occupies Li sites preferentially, compared to Ni^{2+}; this suggests the chemical formula for the Fe-substituted samples as follows: $\left[Li_{1-z}Ni^{2+}_{z-a}Fe^{3+}_a\right]_{inter-slab}$ $\left[Ni^{3+}_{1-y}Fe^{3+}_{y-a}Ni^{2+}_{z+a}\right]_{slab} O_2$. Variations of the trigonal distortion and cation mixing could be estimated from XRD patterns using two factors involving the Bragg line intensity. It is known that the smaller value of the ratio $(I_{006}+I_{102})/I_{101}$, called the R_1-factor, is related to higher hexagonal ordering and the large value of the ratio $R_2 = I_{003}/I_{104}$ is related to the smaller cation mixing. The $Li(Ni_{0.5}Co_{0.5})_{1-y}Fe_yO_2$ cathodes synthesized under mild conditions (sol–gel technique) shows the smallest R_1-factor $[(I_{006}+I_{102})/I_{101}]$ and the largest I_{003}/I_{104}, indicating better hexagonal ordering and less cation mixing, respectively, for $y = 0.1$ (Fig. 5.16). The direction of the c-axis distorted in the $R\overline{3}m$ structure is reflected by the splitting of the (006) and (102) peaks, and (108) and (110) peaks in the XRD patterns (see Fig. 5.12).
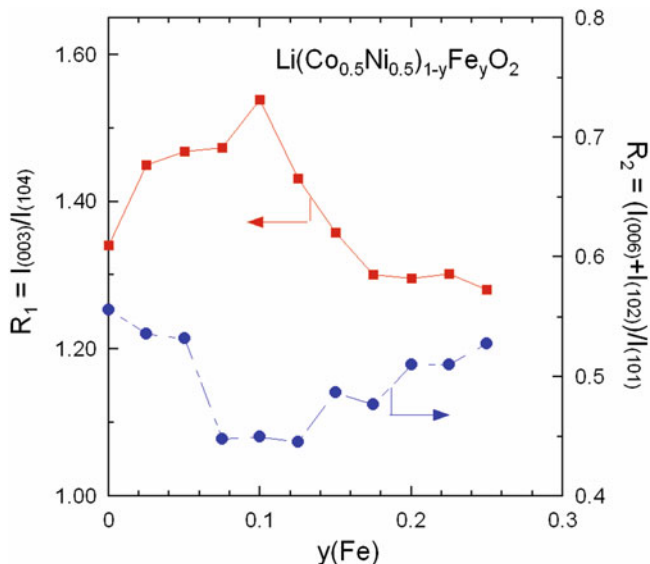
Fig. 5.16 Variation of the R-factors indicating better hexagonal ordering and less cation mixing for $y = 0.1$ in $Li(Ni_{0.5}Co_{0.5})_{1-y}Fe_yO_2$

Since the voltage-composition curves for LCO and LNO are similar, the NCO solid solution could be expected to give a cathode performance similar to that of Li_xCoO_2, but with a significant reduction of cobalt and partly elimination of the Ni^{II} from the lithium layers for $y > 0.3$. It was demonstrated that the Ni^{4+}/Ni^{3+} couple lies about 0.35 eV above the Co^{4+}/Co^{3+} couple, which gives a somewhat larger capacity [102]. Although the capacity of $LiCoO_2$ is about 130 mAh g^{-1}, the capacity of $LiNi_{1-y}Co_yO_2$ with part of the Co substituted by Ni increases to about 180 mAh g^{-1} but the discharge voltage falls slightly (suppression of the H1 $\leftrightarrow$ H2 transformation). This solid solution system, especially the composition $LiNi_{0.8}Co_{0.2}O_2$, appears to replace $LiCoO_2$. A charge–discharge voltage profile for this composition is shown in Fig. 5.17. The $LiNi_{0.8}Co_{0.2}O_2$ electrode showed a high discharge capacity of 200 mAh g^{-1} at 25 °C. Investigations of the physical-chemistry of $LiNi_{1-y}Co_yO_2$ compounds include structure and morphology [101], vibrational spectroscopy [103], magnetism [104, 105], electronic transport [97], nuclear magnetic resonance [106] as a function of the composition. Chebiam et al. [107] showed that cobalt-rich phases tend to lose oxygen on deep lithium extraction due to the overlap of the $Co^{3+/4+}:t_{2g}$ band with the top of the O:$2p$ band in $Li_{1-x}Ni_{1-y}Co_yO_{2-\delta}$.

Thin films $LiNi_{1-y}Co_yO_2$ compounds were also prepared [108]. Highly oriented $LiNi_{0.8}Co_{0.2}O_2$ films grown by pulsed-laser were fabricated for application in microbatteries [109]. Electrochemical titration curve shows a specific capacity of 85 μAh μm^{-1} cm^{-2} at current density 4 μA cm^{-2} in the potential range 2.5–4.3 V.

Fig. 5.17 Typical charge–discharge characteristics of Li//LiNi$_{0.8}$Co$_{0.2}$O$_2$ nonaqueous cells using the electrolyte of composition 1 mol L^{-1} LiClO$_4$ in PC at 25 °C. Charge and discharge were obtained at current densities 0.1 mA/cm^2. LiNi$_{0.8}$Co$_{0.2}$O$_2$ powders were fired at 700 °C for 4 h in air
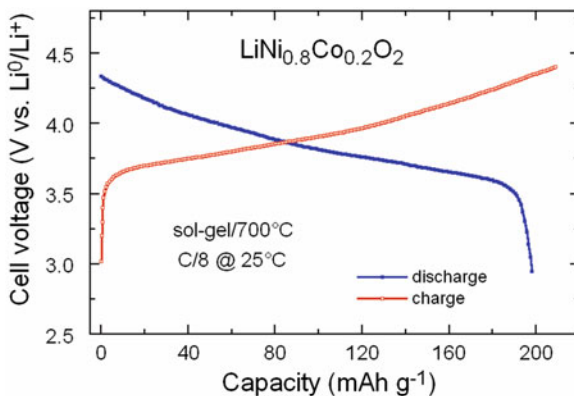
5.3.4   Doped LiCoO$_2$ (d-LCO)

LCO was doped with several elements to stabilize the layered lattice at x(Li) < ½ and extend the specific discharge capacity of LiCo$_{1-y}$M$'_y$O$_2$ [110, 111] Doping elements include M' = Al [112, 113], M' = Mg [99], M' = B [114], M' = Cr [115]. They were mainly prepared by soft-chemistry via dicarboxylic acid-assisted sol–gel method [116, 117]. In this technique, the chelating agent, C$_n$H$_m$O$_4$, with COOH groups, plays the role of oxidant starting from high purity metal acetates dissolved in a minimum volume of distilled water. The concentration of the chelate was adjusted carefully to get a solution with the pH in the range 3–4. The paste was further dried at 120 °C to obtain the dried precursor mass. The decomposition of the precursor was made in air at around 400 °C followed by calcination at 800 °C. Scanning electron microscopy (SEM) studies reveal the nano-structured morphology of the powders. The influence of Al doping on particle size and morphologies has been clearly evidenced [118]. The layered structure of boron-substituted LiCo$_{1-y}$B$_y$O$_2$ is preserved upon a large amount of B^{III} incorporation ($y \leq 0.25$), for which no residual impurity phases were detected [114]. The limit of solubility of boron is also the composition that optimizes the electrochemical properties. Up to $y \leq 0.2$ the boron improves importantly the cycling performance of the battery, as the dopant favors lattice adaptation to the insertion/extraction of Li$^+$ ions and prevents the onset of the structural first-order transition associated with the Verwey transition in Li$_{0.5}$CoO$_2$. Abuzeid et al. [119] reported the synthesis of LiCo$_{0.8}$Mn$_{0.2}$O$_2$ using a wet-chemical method via citric-acid route. This cathode material has the ability to free Li$^+$ ions from its structure by chemical process analogous to the first step of the charge transfer reaction in an electrochemical cell. Both the concentration of Mn^{3+}–Mn^{4+} pairs and that of Mn^{4+}–Mn^{4+} pairs formed in the delithiation process have been determined, together with that of the Mn^{3+}–Mn^{3+} pairs. The results indicate a random distribution of the Li ions that are removed from the matrix upon delithiation, which then undergo a diffusion process. Testing the material as cathode in lithium batteries revealed a capacity of ~170 mAh g^{-1} with lower polarization and high coulombic efficiency [120].
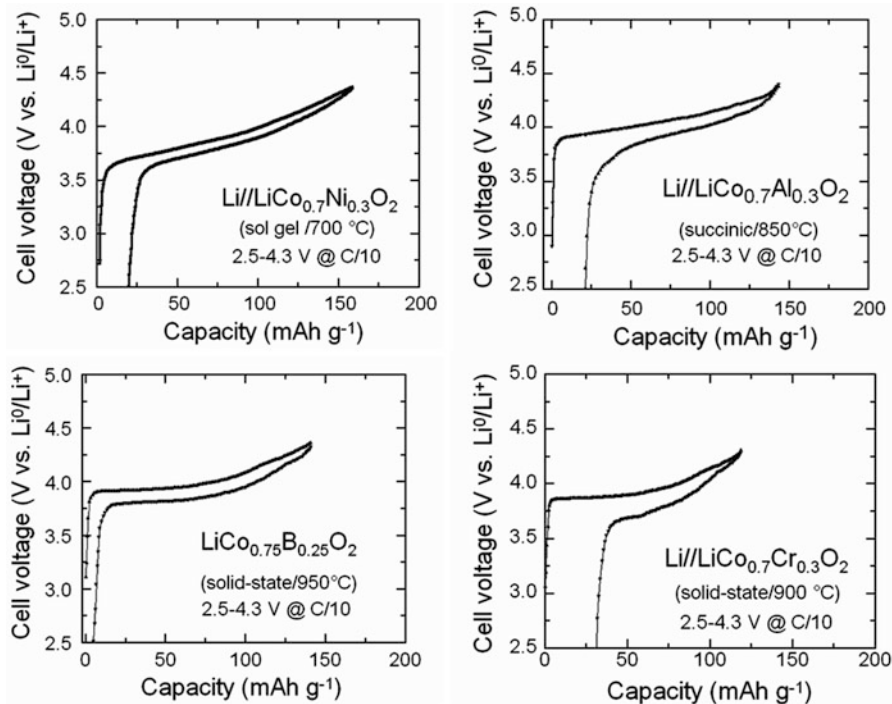
Fig. 5.18 Electrochemical features of Li//LiCo$_{1-y}$M$'_y$O$_2$ cells during the first charge–discharge cycle carried out in the range 2.5–4.4 V at C/10 rate. (**a**) M$'$ = Ni, (**b**) M$'$ = Al, (**c**) M$'$ = B, and (**d**) M$'$ = Cr

In Fig. 5.18, the electrochemical features of synthesized LiCo$_{0.7}$M$'_{0.3}$O$_2$ (M$'$ = Ni, Al, B and Cr) layered oxides are compared. The electrochemical features of the layered LiCo$_{0.7}$Ni$_{0.3}$O$_2$, LiCo$_{0.7}$Al$_{0.3}$O$_2$, and LiCo$_{0.65}$B$_{0.35}$O$_2$, oxides resemble to that of LiCoO$_2$. Replacing a small amount of Co demonstrates the disappearance of the voltage plateau at 3.85 V in the charge curve. This is attributed to the absence of the semiconductor-metal transition with M$'$ substitution [121]. Chemical substitution of products improves electrochemical properties for Al- and Ni-based materials, which exhibit good capacity retention. The efficiency in maintaining capacity retention is observed over a large number of cycles without sacrificing initial reversible capacity. However, the electrochemical profile of the LiCo$_{0.7}$Cr$_{0.3}$O$_2$ cell displays a large capacity fading attributed to the structural distortion upon substitution [115]. The electrochemical profiles of Li//LiCo$_{1-y}$B$_y$O$_2$ cells including various levels of boron substitution (0.05 ≤ y ≤ 0.35) in their positive electrode provide very low polarization during charge–discharge cycling, with capacity over 130 mAh g^{-1} when charged up to 4.3 V vs. lithium anode. Capacity of the LiCoO$_2$ doped with 15 % boron remains over 125 mAh g^{-1} after 100 charge–discharge cycles. It appears that a less electrolyte decomposition occurs with boron or aluminum substitution in LiNiO$_2$ and LiCoO$_2$ cathodes in lithium batteries [99].

5.3.5 $LiNi_{1-y-z}Co_yAl_zO_2$ (NCA)

Among the Ni-rich layered compounds, $LiNi_{1-y-z}Co_yAl_zO_2$ (NCA) exhibits enhanced electrochemical performance compared with non Al-doped $LiNi_{1-y}Co_yO_2$ mixed materials because of its structural and thermal stability [122–125]. The specific composition $LiNi_{0.80}Co_{0.15}Al_{0.15}O_2$ is currently used in the 85-kWh battery pack to power the EV Roadster by Tesla at high speed. Note that NCA-type materials are currently used in SAFT commercial batteries for various applications (EV, HEV, space, military, etc.) [126]. Majumdar et al. [127] synthesized NCA powders via wet-chemical route using metal acetates and aluminum nitrate. The electrochemical features carried out in the potential range 3.2–4.2 V at a current density 0.45 mA cm^{-2} showed a specific capacity of ~136 mAh g^{-1}. NCA prepared by a co-precipitation method showed a quasi-ideal lamellar structure with less than 1 % extra-nickel ions in the interslab space [92]. Bang et al. [124] investigated the structural change of the delithiated cathode $LiNi_{0.80}Co_{0.15}Al_{0.05}O_2$ during thermal decomposition, the XRD analysis was carried out with different states-of-charge (SOCs). As the SOC increases, the (018) and (110) Bragg lines at $2\theta = 65°$ move toward lower higher angles, respectively. An increase in the distance between these reflections indicated an increase in the c/a ratio of the NCA lattice [128]. Improvement of the electrochemical performance at high temperature (60 °C) was obtained by coating the NCA powders with metal oxides. Cho et al. [129, 130] stabilized the surface of nanoparticles by SiO_2 and TiO_2 dry coating. Surface modification of NCA nonapowders has been also obtained with various other coatings such as $Ni_3(PO_4)_2$ [131], AlF_3 [132], $Li_2O-2B_2O_3$ (LBO) glass [133], and carbon [134]. Enhancement of the capacity retention (169 mAh g^{-1} at current density 360 mA g^{-1}) at high temperature of $LiNi_{0.80}Co_{0.15}Al_{0.05}O_2$ has been obtained with a 2 wt% LBO coating [133]. Belharouak et al. [135] studied the thermal degradation of deintercalated NCA samples. They reported that the oxygen release from these delithiated powders was associated with the occurrence of several structural transformations, ranging from the $R\overline{3}m \rightarrow Fd3m$ (layered $\rightarrow$ spinel) transition to the $Fd3m \rightarrow Fm3m$ (spinel $\rightarrow$ NiO-type) transition.

5.3.6 $LiNi_{0.5}Mn_{0.5}O_2$ (NMO)

Layered, monoclinic $LiMnO_2$ is isostructural with $LiCoO_2$ but transforms on cycling at 3–4 V vs. Li^0/Li^+ to more thermodynamically stable spinel phase. Cation doping (e.g., Ni^{2+} or Cr^{3+}) can be used to stabilize the layered phase with some success. The layered oxide $LiNi_{0.5}Mn_{0.5}O_2$ (NMO) was reported to be a promising positive electrode material [136, 137]. $LiNi_{0.5}Mn_{0.5}O_2$ adopts a hexagonal unit cell (α-NaFeO$_2$-like). XANES experiments have demonstrated that transition-metal ions adopt the Ni^{3+} and Mn^{4+} state with a small fraction of divalent Ni^{2+} ions. The manganese remaining in the +4 valence state at all times prevents the instabilities
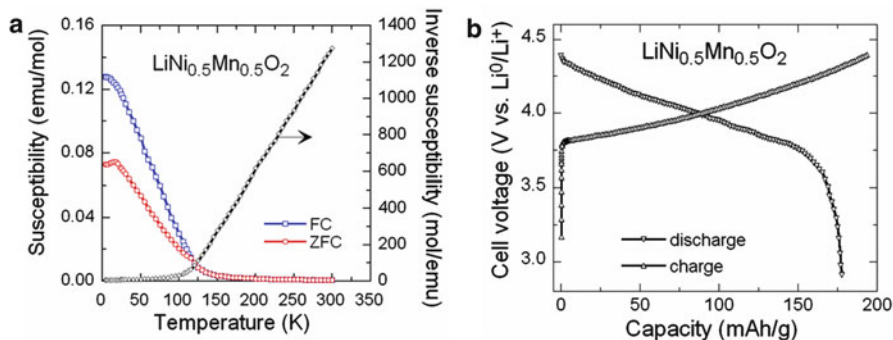
Fig. 5.19 (**a**) Temperature dependence of the magnetic susceptibility of $LiNi_{0.5}Mn_{0.5}O_2$ powders for zero-field cooling (ZFC) and field-cooling (FC). (**b**) Charge and discharge curves of the $Li//LiNi_{0.5}Mn_{0.5}O_2$ cell with a current density of 0.12 mA/cm^2 and cutoff voltage of 2.6 and 4.2 V. The cathode material was synthesized by citric acid assisted sol–gel method

associated with Jahn–Teller Mn^{3+} ions. This material shows a reversible capacity 150 mAh g^{-1} in the voltage range 2.5–4.3 V and exhibits the superior characteristics of a larger capacity than $LiMn_2O_4$ and better thermal stability than $LiNiO_2$. Structural analysis have shown that the lattice parameters of $LiNi_{0.5}Mn_{0.5}O_2$ are $a = 2.896$ Å and $c = 14.306$ Å and the chemical composition can be expressed by referring to the Wyckoff positions $3a$ and $3b$ of the space group $R\overline{3}m$ as $[Li_{0.92}Ni_{0.07}]_{3a}[Li_{0.08}Mn_{0.5}Ni_{0.43}]_{3b}O_2$. Figure 5.19a shows the magnetic properties of $LiNi_{0.5}Mn_{0.5}O_2$ [138] with the plot of the molar spin susceptibility, $\chi(T)$ as a function of the temperature in the range 4–300 K. A cusp in $\chi(T)$ is observed close to 15 K that is similar to the spin-glass behavior reported for $LiNiO_2$ [139, 140]. A large deviation between ZFC and FC curves below 100 K indicates the existence of ferromagnet. The ferromagnetic interaction is associated with the random occupancy of $3a$ and $3b$ sites by 7 % Ni^{2+} and 50 % Mn^{4+}, respectively. The 180° Ni^{2+}-O-Mn^{4+}-O-Ni^{2+} superexchange interaction is assumed to be ferromagnetic in $LiNi_{0.5}Mn_{0.5}O_2$. In this layered compound the almost linear 180° M_{3a}-O-M_{3b}-O-M_{3a} bond is expected to be stronger than the interlayer 90° M_{3b}-O-M_{3b} bond when the $3a$ site is partially occupied by M cations [139]. Figure 5.19b shows the charge and discharge curves of the $LiNi_{0.5}Mn_{0.5}O_2$ cell with a current density of 0.12 mA cm^{-2} and cutoff voltage of 2.6 and 4.2 V. This electrochemical profile indicates that the lithium deintercalation process in $LiNi_{0.5}Mn_{0.5}O_2$ proceeds via a single-phase reaction.

5.3.7 $LiNi_{1-y-z}Mn_yCo_zO_2$ (NMC)

In search of high-power lithium-ion batteries with excellent calendar life and better thermal abuse tolerance to replace the $Li//LiCoO_2$ system, the new chemistry $Li(Ni,Mn,Co)O_2$ (NMC) was first synthesized by Liu et al. [141]. These compounds of various compositions, which look like the simple solid solution

**Fig. 5.20** The triangular
phase diagram of the
$LiCoO_2$-$LiNiO_2$-$LiMnO_2$
solid solution
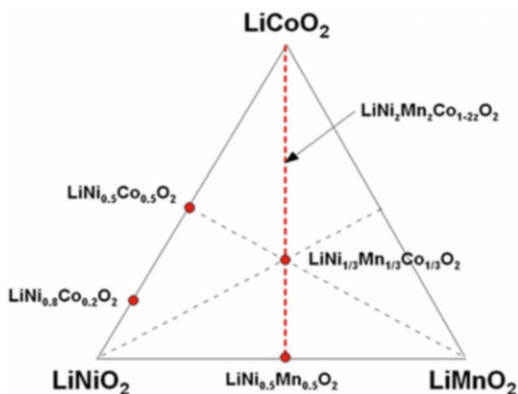
$LiCoO_2$-$LiNiO_2$-$LiMnO_2$ (Fig. 5.20), have been intensively studied with ultimate goals of large enhancement of the thermal and structural stability and appreciable increase of the capacity retention because the combination of nickel, manganese, and cobalt can provide many advantages. The $LiNi_{1-y-z}Mn_yCo_zO_2$ compounds crystallize with the α-$NaFeO_2$-type structure ($R\overline{3}m$ space group). The pioneering work of the Dahn's group demonstrated the high performance of the $Li//LiNi_yMn_yCo_{1-2x}O_2$ and suggested the valence state of transition-metal cations such as divalent (Ni^{2+}), trivalent (Co^{3+}) and tetravalent (Mn^{4+}), respectively [142, 143]. Note that to keep the charge neutrality and avoid the Mn^{3+} Jahn–Teller ions, the amount of Ni and Mn ions must be equal. It was reported that $LiNi_yMn_yCo_{1-2x}O_2$ showed a specific capacity of 160 mAh g^{-1} over 2.5–4.4 V [144] and the thermal behavior of charged $LiNi_yMn_yCo_{1-2x}O_2$ was milder than that of charged LCO and LNO [145]. There are many factors that influence the electrochemical features of $LiNi_{1-y-z}Mn_yCo_zO_2$ such as synthesis preparation, structural defects, morphology, composition, operation voltage domain. Lee et al. [146] have investigated the defect chemistry and doping effects of NMCs in terms of energetics and dynamics with special attention of the antisite pair defects. Properties of NMCs were summarized in several review papers [147–149]. NMR studies have evidenced for a nonrandom distribution of the transition-metal cations in $LiNi_{1-x-y}Mn_xCo_yO_2$ [150]. The insulator-to-metal transition observed with $LiCoO_2$ disappeared at $y \geq 0.2$ due to the loss of contact between Co ions that interrupts the cooperative effect. Various synthetic methods have been applied to elaborate $LiNi_{1-y-z}Mn_yCo_zO_2$ compounds such as traditional solid-state reaction [151, 152], supercritical water method [153], sol–gel technique [154], co-precipitation synthesis [155–157], spray-drying method [121, 158, 159], radiated polymer gel method [160], solvent evaporation method [161], molten-salt synthesis [162], polymer template route [163], and Pechini method [164]. Among these synthetic methods, co-precipitation and sol–gel route have been found powerful, economic, and easy for large scale fabrication, because the TM ions are precipitated in an homogeneous manner and oxidized in the aqueous solution at the molecular level. Fujii et al. [165] indicated that high calcination temperature results

in the formation of vacancies in the TM slabs, lowers the specific capacity and degrades the cycle performance. The optimum calcination temperature is 900 °C in order to obtain the electrochemically active and dense packed oxide particles.

Electrochemical performance of $LiNi_{1-y-z}Mn_yCo_zO_2$ cathode materials were improved by doping cations [166, 167] and anion substitution of fluoride for oxygen [168]. The long-range and local structure and cationic environment in $LiNi_{1-y-z}Mn_yCo_zO_2$ were studied by FTIR and EPR spectroscopy [169]. Cation ordering was investigated by using a combination of ^6Li magic angle spinning (MAS) nuclear magnetic resonance (NMR) spectroscopy and neutron pair distribution function (PDF) analysis [150]. For $Li[Ni_xMn_yCo_z]O_2$ lamellar compounds, the electronic conductivity is not a problem but these materials have poor cycling stability at high rate or high cutoff voltage, which limits their use to portable applications. Aurbach et al. [170] have suggested that the capacity retention is strongly dependent on the surface chemistry of the particles because of resistive SEI layer. That is why many attempts have been made to protect the surface of NMC materials with metal oxides such as Al_2O_3, TiO_2, ZrO_2, and MgO, or other compounds such as $FePO_4$, $LiFePO_4$, and $Li_4Ti_5O_{12}$ [83]. The improvement of the electrochemical performance due to the crystallization of the surface layer can be understood as follows. First, the electronic conductivity is affected by the structural disorder. This has been evidenced by transport experiments that have shown an increase of conductivity when the calcination temperature used in the synthesis process increases from 800 up to around 1000 °C, owing to improved crystallinity of the materials [164]. In fact, a high crystallinity is essential to obtain good electrical conductivity. In another approach, direct UV-assisted conformal coating of poly(tris(2-(acryloyloxy)ethyl) phosphate) (PTAEP) gel polymer electrolyte on as-formed $LiNi_{1/3}Mn_{1/3}Co_{1/3}O_2$ (NMC) cathode is quite a new process. A smooth and continuous PTAEP coating layer with thickness 20 nm was obtained, which improved the 4.6 V cycling performance, without impairing discharge capability [171]. The authors, however, were too optimistic when claiming that it suppressed the exothermic reaction. It only shifted the exothermic peak temperature from 284 to 294 °C and reduced the exothermic peak from 649 to 576 J g^{-1}. This is, however, a new conformal coating strategy that has to be explored on other electrodes.

Nowadays, the magic composition $LiNi_{1/3}Mn_{1/3}Co_{1/3}O_2$ with hexagonal structure, first introduced by the Ohzuku's group in 2001, has attracted more significant interest as a candidate of cathode materials because the good stability during cycling even at elevated temperature, and high reversible capacity [155]. The lithium excess cathode $Li_{1+x}(Ni_{1/3}Mn_{1/3}Co_{1/3})_{1-x}O_2$ was found to exhibit better cyclability and rate capability than the stoichiometric material up to a cutoff charge voltage of 4.6 V vs. Li^0/Li$^+$ [172–174]. Ligneel found that NMC structural stability [174]. Zhang et al. [173] have explored the co-precipitation route to synthesize the $Li_{1+x}(NMC)_{1-x}O_2$ powders and optimize its structure by adjusting one parameter of the synthesis, namely the lithium–transition metal ratio (κ), so as to minimize the cation mixing. The synthesis of NMC powders was performed by a hydroxide route using transition-metal hydroxide and lithium carbonate as with Li excess
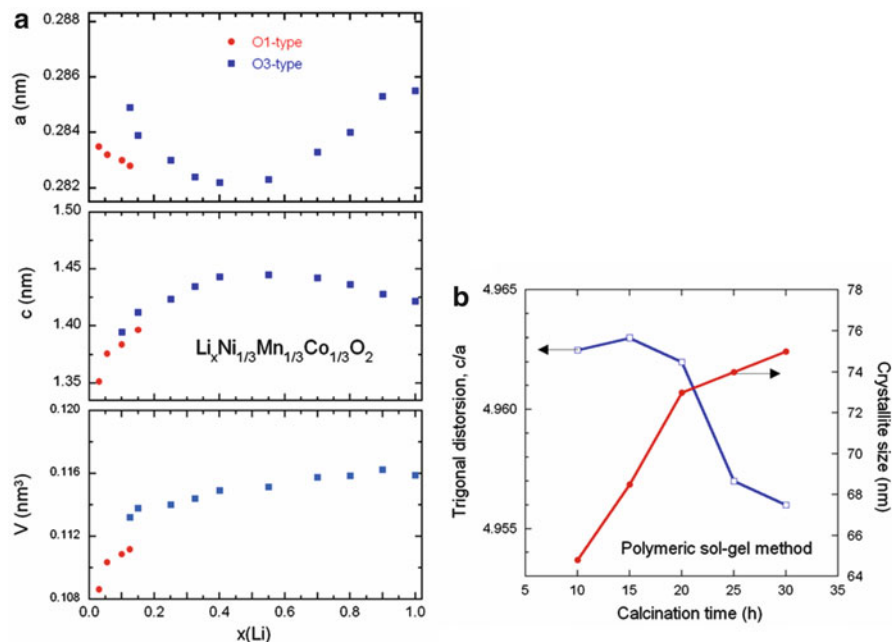
Fig. 5.21 (**a**) Evolution of the lattice parameters vs. $x(Li)$ in $Li_xNi_{1/3}Mn_{1/3}Co_{1/3}O_2$. Powders were prepared by citrate gel method with molar ratio $Li/(Ni + Mn + Co) = 1$. (**b**) Evolution of the trigonal distorsion, i.e., the c/a ratio and particle size of $Li_xNi_{1/3}Mn_{1/3}Co_{1/3}O_2$ powders as a function of the calcination time at the optimum temperature of 900 °C

$0.04 \leq x \leq 0.12$ shows a strong starting materials. The final products were fired at 950 °C for 10 h in air. The samples described here were obtained with nominal values: $\kappa = Li/M = 1.05$ (sample-A) and $\kappa = 1.10$ (sample-B) with $M = Ni + Mn + Co$. The Rietveld refinement of the XRD spectra and the analysis of the magnetic properties showed that the concentration of cation mixing for sample-A and sample-B were below 2 %. Figure 5.21 shows the evolution of the structural properties of $Li_xNi_{1/3}Mn_{1/3}Co_{1/3}O_2$ powders prepared by the citrate gel method with metal molar ratio $Li/(Ni + Mn + Co) = 1$. The evolution of the lattice parameters vs. $x(Li)$ in $Li_xNi_{1/3}Mn_{1/3}Co_{1/3}O_2$ displays the two structural O1- and O3-phase. The curves of the trigonal distortion measured from the c/a ratio, and particle size as a function of the calcination temperature for $Li_xNi_{1/3}Mn_{1/3}Co_{1/3}O_2$ show that heat treatment for 20 h is sufficient. The electrochemical features of are displayed in Fig. 5.22a for $Li_{1+x}(NMC)_{1-x}Co_{1/3}O_2$ powders synthesized by the co-precipitation method with $\kappa = 1.05$. Results show a loss rate of 0.15 % per cycle for the NMC electrodes synthesized by co-precipitation method. More than 95 % of its initial capacity was retained after 30 cycles in the cutoff voltage of 3.0–4.3 V at 1 C-rate. Note that a cation mixing below 2 % can be considered as the threshold for which the electrochemical performance does not change for NMC. The diagram of the discharge capacity against thermal stability for a series of NMC cathode materials
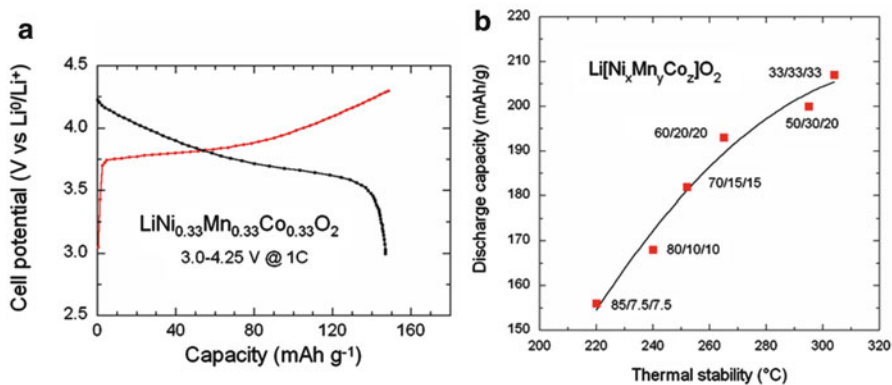
Fig. 5.22 (**a**) The electrochemical features of $Li_{1+x}(NMC)_{1-x}Co_{1/3}O_2$ powders synthesized by the co-precipitation method. The structure was optimized by adjusting the lithium–transition metal ratio to $\kappa = Li/M = 1.05$. Results indicated a rate of 0.15 % per cycle for the NMC electrodes. (**b**) Diagram discharge capacity against thermal stability measured by the exothermic peak temperature for a series of $LiNi_xMn_yCo_zO_2$ cathode materials. The number indicates the amount of Ni/Mn/Co

is shown in Fig. 5.22b. The number indicates the amount of Ni/Mn/Co in $LiNi_xMn_yCo_zO_2$. This graph shows clearly that the more stable cathode is $LiNi_{0.33}Mn_{0.33}Co_{0.33}O_2$.

5.3.8 Li$_2$MnO$_3$

Lithium manganate Li_2MnO_3 attracts an ever-growing attention of researchers and is still the object of debates since, among the family of manganese oxides, it is one of the most interesting compounds from the view point of electrochemical behavior and structural evolution upon charge/discharge [175–179]. Li_2MnO_3 possesses an O3-type structure that can be represented in conventional layered $LiMO_2$ notation as $Li_{3a}[Li_{1/3}Mn_{2/3}]_{3b}O_2$, where interslab octahedral sites are only occupied by Li^+-ions while Li^+ and Mn^{4+}-ions (in a ratio of 1:2) occupy slab octahedral sites, and $3a$ and $3b$ refer to the octahedral sites of the trigonal lattice [180]. In other words, in Li_2MnO_3, 1/3 of the Mn-ions in the transition metal layer is replaced with Li. Layers of lithium ions and alternating layers of manganese ions are separated from one another by layers of cubic-close packed oxygen planes, thus resembling the ideal layered structure of $LiCoO_2$. It should be noted that Li_2MnO_3 is an integrated part of the so-called high-energy cathode $xLi_2MnO_3\cdot(1-x)Li[M]O_2$ materials ($M =$ Mn, Ni, Co) for Li-ion batteries that provide reversible capacities >200 mAh g^{-1} [181]. In these materials, Li_2MnO_3 component plays an important role of supplying lithium and stabilizing the electrode structure. Li_2MnO_3 is rich in mobile Li^+ ions and theoretically can deliver a high capacity of 460 mAh g^{-1} for

total Li extraction when charged up to 4.6 V. However, manganese cannot be oxidized beyond +4 in an octahedral environment and Li_2MnO_3, especially in its microcrystalline form, is considered electrochemically inactive for lithium insertion and extraction. It was shown that Li^+ extraction from Li_2MnO_3 is possible not by oxidation of Mn^{4+} but by other mechanisms. They may involve simultaneous removal of oxygen (Li_2O) to balance the charge [182] or exchange of Li^+ ions by protons generated from oxidation reactions of the nonaqueous electrolyte solutions at elevated temperatures [183]. Actually, Li_2MnO_3 becomes electrochemically active in electrodes comprising its nano-sized particles and these electrodes demonstrate much higher electrochemical activity in terms of capacity and cycling behavior [178]. This can be due to decreasing the potential of the Li^+-ions extraction from the host structure in the first charge associated with the higher surface-to-volume ratio, much shorter distances for the electrons and the Li-ion transport in nanoparticles, the increased surface concentration of the electrochemically active sites, and with a better accommodation of strain during Li^+ extraction/insertion. Recently, Okamoto related a substantial decrease of the potential of the Li^+-ions extraction to the increasing concentration of oxygen vacancies in Li_2MnO_3, which activate the Mn sites as the redox centers in the Li deintercalation reaction [184]. There are many reports [185, 186] dedicated to structural transformations of layered cathode materials $LiMO_2$ for Li-cells (M = transition metal, like Mn, Ni, Co) from the layered to spinel-type ordering upon Li electrochemical or chemical deintercalation. Amalraj [179] reported this structural transformation upon charging Li_2MnO_3 electrodes that comprises micro- or nano-sized particles at high anodic potentials (4.6–4.7 V). Ito et al. [187] have shown that in the first charge of $xLi_2MnO_3\cdot(1-x)Li[M]O_2$ integrated materials, the formation of the spinel-type ordering started just at the potential plateau around 4.5 V, at the same time as the electrochemical activation of Li_2MnO_3 ($Li_2MnO_3 \rightarrow Li_2O + MnO_2$) occurs at this potential. On the other hand, we have established that in the above materials, in which the structurally compatible Li_2MnO_3 (layered monoclinic) and $LiMO_2$ (layered rhombohedral) components are closely interconnected with one another and coexist side by side in the structure, partial layered-to-spinel transition occurred even at the early stages of the first charge (Li^+-extraction), at 4.1–4.4 V [188]. In this potential range, the Li^+ ions are extracted (deintercalated) only from the electrochemically active $LiMO_2$ component, while Li_2MnO_3 remains inactive until 4.5 V (Fig. 5.23). Therefore one can suggest that $LiMO_2$ is "responsible" for the observed partial transformation of the layered-type to spinel-type structural ordering in electrodes comprising $xLi_2MnO_3\cdot(1-x)Li[M]O_2$ materials. This transformation is supposed to be due to the partial irreversible migration of transition metal cations into interlayer Li sites by the electrochemical charging the electrode or by chemical delithiation (leaching) of the layered material in acidic media [175, 178, 183, 185].

The structural transformations from the layered-type to spinel-type ordering was investigated at various states-of-charge of Li_2MnO_3 electrodes, even at the early stages around 4.3 V far beyond the electrochemical decomposition of $Li_2MnO_3,$ and at 4.5 V (potential plateau) where it decomposes into Li_2O and MnO_2 [189]. This
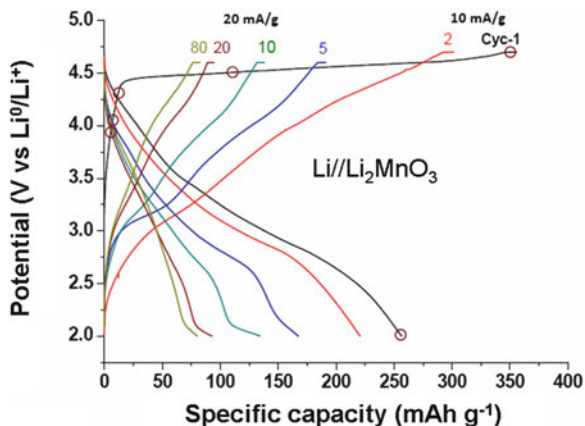
Fig. 5.23 Typical potential profiles measured in the ranges of 2.0–4.7 V (first 2 cycles) and 2.0–4.6 V (rest of the cycles) from a Li_2MnO_3 electrode at 30 °C in coin-type cells. Cycle numbers are indicated on the curves. The cycling mode was CC–CV, potentiostatic steps were 1 h at 4.7 V and 0.5 h at 4.6 V. The first 2 cycles were performed by applying the current density of $i = 25$ mA g^{-1}. For cycles 3–100 the current density was $i = 20$ mA g^{-1} and for the subsequent cycles $i = 10$ mA g^{-1}. Empty circles on the charge–discharge profiles of the first cycle indicate potentials, at which electrochemical cells were terminated and Li_2MnO_3 electrodes studied for possible structural transformations
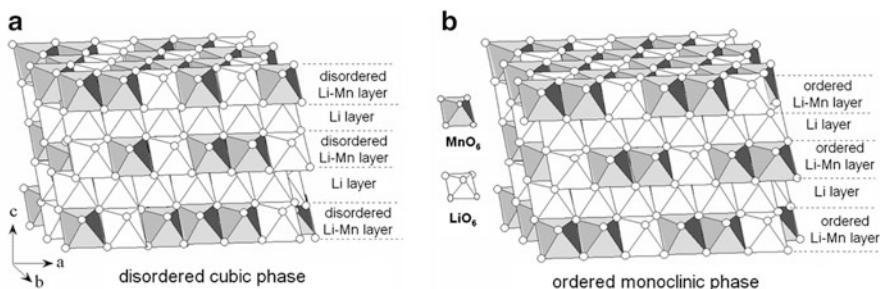
Fig. 5.24 (**a**) Schematic representation of the Li_2MnO_3 crystallographic structures showing the α-phase with randomly distributed cation sites in the Li-Mn layers, (**b**) the β-phase corresponding to the case where the cations are ordered

layered-to-spinel transformation was examined by means of X-ray and electron diffraction techniques, Raman spectroscopy, and the study of the magnetic properties of Li_2MnO_3, which is an efficient tool to probe structural ordering. The novelty of this work is that layered-to-spinel structural transformations were detected and studied at the initial states-of-charge, prior to the electrochemical activation of Li_2MnO_3 electrodes. In addition, the prior works related to this cathode material miss the polymorphism of Li_2MnO_3 that is able to crystallize in α- and β-phases (Fig. 5.24) depending on the sintering temperature during the synthesis process [190].

5.3.9 Li-Rich Layered Compounds (LNMC)

Novel Li-rich layered cathode materials, the "layered-rocksalt" Li $[Li_xNi_yCo_yMn_{1-x-y}]O_2$ frameworks (LNMC) have received great attention because of their ability to deliver capacities of 250 mAh g^{-1} when electrochemically activated at 4.6 V [191–205]. Layered-rocksalt compounds can be regarded, in a homogeneous phase approach, as a solid solution series between $Li[Li_{1/3}Mn_{2/3}]O_2$ and $LiNi_zCo_{1-z}O_2$ [191] as shown by the phase diagram in Fig. 5.25 and on the other hand it is regarded, in a two-phase approach as a kind of composite electrode with nanoclusters of Li_2MnO_3 and $Li(Ni,Co)O_2$ in localized regions [192]. Various synthesis techniques used to fabricate high-capacity LNMC composite materials include ion-exchange reaction [206], solid-state reaction of metal hydroxide with calcination at 900 °C for 24 h [207], co-precipitation method [208], sol–gel method [209], molten salt method [210], and template-free method [211].

Figure 5.26 compares the charge–discharge profiles of the Li-rich layered compounds of composition $Li_{1.134}Ni_{0.3}Mn_{0.566}O_2$ and $Li_{1.2}Ni_{0.13}Mn_{0.54}Co_{0.13}O_2$ synthesized by sol–gel method assisted by citric acid as chelating agent. Measurements were carried out at $C/10$ rate in the potential range 4.8–2.0 V. The electrochemical curves exhibit two regions (I and II) during the first charge (separated by a dashed line in Fig. 5.26). The region (I), below 4.6 V, corresponds to the oxidation of the transition-metal cation (TM) to tetravalent state M^{4+}, while the plateau (region II) at around 4.6 V corresponds to an oxidation of O^{2-} ions and the irreversible loss of oxygen from the lattice [212]. The oxygen loss leads to a lowering of the oxidation states of the TM ions at the end of the first discharge, which makes easier the reversibility of subsequent cycles. As reported by Wu and Manthiram [213], the irreversible loss of oxygen from the LNMC framework can be reduced by a substitution of small amount of Al^{3+} for Li^+ or F^- for O^{2-}, which

Fig. 5.25 Ternary phase diagram of the "layered-rocksalt" $Li[Li_{1/3}Mn_{2/3}]O_2$-$LiCoO_2$-$LiNiO_2$ solid solution systems
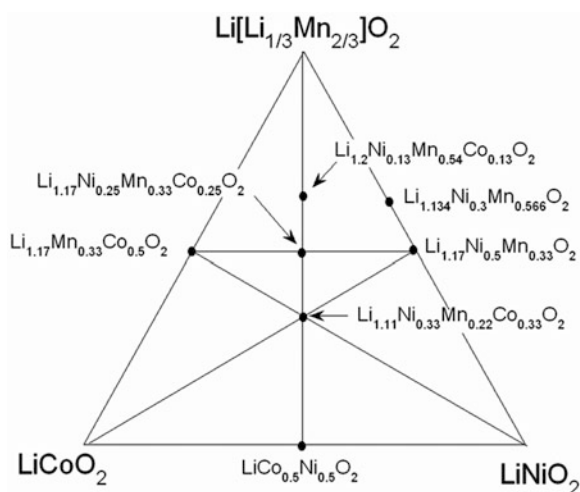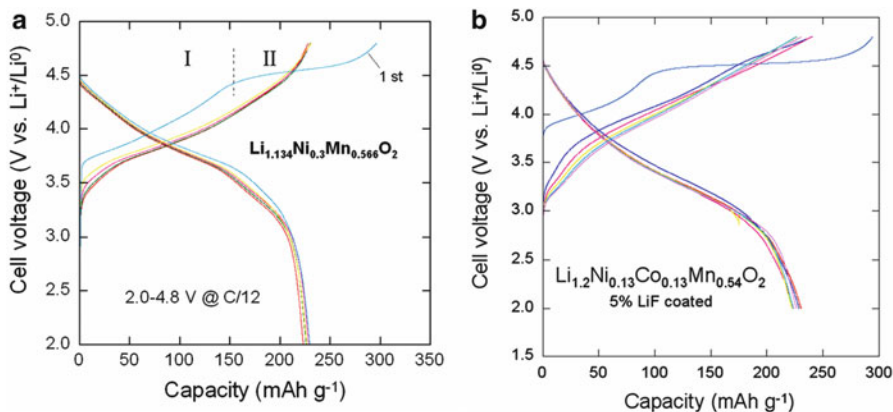
Fig. 5.26 Charge–discharge curves of Li-rich layered-rocksalt composite electrodes. (**a**) $Li_{1.134}Ni_{0.3}Mn_{0.566}O_2$ and (**b**) 5 % LiF-coated $Li_{1.2}Ni_{0.13}Mn_{0.54}Co_{0.13}O_2$. Measurements were carried out in the galvanostatic mode at $C/12$ rate in the potential range 2.0–4.8 V

lowers significantly the irreversible capacity loss (ICL). High capacity of $Li[Li_{(1-x)/3}Mn_{(2-x)/3}Ni_{x/3}Co_{x/3}]O_2$ can be obtained by surface modification with Al_2O_3. For instance, surface modified $Li[Li_{0.2}Ni_{0.13}Mn_{0.54}Co_{0.13}]O_2$ shows a remarkably high capacity of 285 mAh g^{-1} with an ICL of 41 mAh g^{-1} and good rate capability [213]. Mechanisms associated with the plateau observed at high voltage for the overlithiated $Li_{1.12}(Ni_{0.425}Mn_{0.425}Co_{0.15})_{0.88}O_2$ system have been discussed by Tran et al. [214].

$Li(Li_{0.17}Ni_{0.2}Co_{0.05}Mn_{0.58})O_2$ particles synthesized by a spray-drying method were modified subsequently with CeO_2 nanoparticles, which results in smaller surface charge transfer resistance and larger discharge capacity [195]. Fluorine doping in $Li_2MnO_3 \cdot LiMO_2$ can create polaron states in the Li_2MnO_3 lattice with a migration energy barrier about 0.27 eV. The polaron state is strongly trapped by fluorine atom, which decreases the efficiency of the doping effect to enhance the electronic conductivity [196]. Novel $Li_{1.2}Mn_{0.5}Co_{0.25}Ni_{0.05}O_2$ microcube prepared through a simple binary template method with calcination at 800 °C [205] providing high reversible discharge capacities of 208 mAh g^{-1} at a current density of 200 mA g^{-1}. In general, owning to oxygen extraction at the first cycle and insulation phase of Li_2MnO_3, the pristine Li-rich layered cathode materials experience high irreversible capacity loss at the first cycle, accompanied with gradual capacity fade and poor rate capability during cycling [196]. The surface modification [215], acid treatment [216], doping [217] as well as blending with other cathode materials [218] have been found to alleviate the irreversible capacity loss at the first cycle. In particular, the irreversible capacity loss at the first cycle was eliminated by blending with other lithium insertion hosts, such as $Li_4Mn_5O_{12}$, LiV_3O_8, V_2O_5 [219].

5.3.10   Other Layered Compounds

5.3.10.1   Mn-Based Oxides

The difficulties met with $LiMn_2O_4$ spinel have also motivated the investigation of several non-spinel manganese oxides [220]. Although $LiMnO_2$ obtained by conventional synthesis procedures adopts an orthorhombic rock-salt structure (*Pmmn* S.G.), in which the oxygen array is distorted from the ideal cubic close packing [221], layered (monoclinic) $LiMnO_2$ isostructural with the layered $LiCoO_2$ (O3 structure) can be obtained by an ion-exchange of $NaMnO_2$ [222] or by a partial substitution of Mn by Cr or Al [223]. Unfortunately, both the orthorhombic and the monoclinic $LiMnO_2$ with a close-packed oxygen array tend to transform to spinel-like phase that is completed within a few charge–discharge cycles [224]. In this regard, $Na_{0.5}MnO_2$—designated as $Na_{0.44}MnO_2$ in the literature—adopting a non-close-packed tunnel structure has drawn some attention as it does not transform to spinel-like phases and shows extraordinary structural stability to temperatures as high as 300 °C [225, 226]

However, only a small amount of lithium could be extracted from the ion-exchanged sample $Na_{0.5-x}Li_xMnO_2$ although additional lithium could be inserted into $Na_{0.5-x}Li_xMnO_2$. Therefore, it is not attractive for lithium-ion cells fabricated with carbon anodes. Nevertheless, it has been shown to be a promising candidate for lithium polymer batteries employing metallic lithium anode [225]. Additionally, amorphous manganese oxides have been shown to exhibit high capacity (300 mAh g^{-1}) with good cyclability [227]. However, the capacity occurs over a wide voltage range extending from 4.3 to 1.5 V with a continuously sloping discharge profile and not much lithium could be extracted from the initial material. Therefore these amorphous oxides are not attractive for lithium-ion cells fabricated with carbon anodes. However, they may become viable with the development of new lithium-containing counter-electrodes.

5.3.10.2   Chromium Oxides

$LiCrO_2$ also crystallizes in the O3 structure of $LiCoO_2$. Although one would expect $Li_{1-x}CrO_2$ to exhibit good structural stability due to the strong preference of Cr^{3+} ions for octahedral sites, it is difficult to extract lithium from $LiCrO_2$. However, a number of chromium oxides such as Cr_2O_5, Cr_6O_{15}, and Cr_3O_8 having a Cr oxidation state of $\geq 5+$ show high capacities and energy densities as high as 1200 mWh g^{-1} above a cutoff voltage of 2 V [228]. Also, amorphous Cr_3O_8 has been found to show high energy density with good rechargeability [229]. However, the synthesis of these oxides generally requires decomposition of CrO_3 in an autoclave or under high oxygen pressure and the products are often contaminated with non decomposed CrO_3. Additionally, amorphous $CrO_{2-\delta}$ ($0 \leq \delta \leq 0.5$) synthesized under ambient conditions by a reduction of potassium chromate solution with

borohydride followed by heat treatment at moderate temperatures have been shown to exhibit >150 mAh g^{-1} capacity [230]. However, the absence of lithium in these materials makes them unsuitable to be employed with carbon anodes in lithium-ion cells.

5.3.10.3   Iron-Based Oxides

Iron oxides offer significant advantages compared to other $3d$-transition-metal oxides from both cost and toxicity points of view. Although LiFeO$_2$ obtained by conventional procedures adopts the cubic structure ($Fm3m$ S.G.), the O3-type layered α-LiFeO$_2$ can be obtained by following the same procedure as in the case of LiMnO$_2$, i.e., by ion-exchange reactions of NaMO$_2$. Unfortunately, the layered LiFeO$_2$ does not exhibit good electrochemical properties as the high spin Fe^{3+}:$3d^5$ ion having no particular preference for octahedral coordination tends to migrate to the lithium planes via the neighboring tetrahedral sites [231]. The cubic phase synthesized via solid state reaction exhibits well-formed crystallites of 0.55 μm size. Magnetic measurements have evidenced that α-LiFeO$_2$ exhibits deviation from the Curie–Weiss law with $\mu_{eff} << 5.9\ \mu_B$ at room temperature. The cationic disorder seems to affect the magnetic properties. This compound is expected to belong to the class of Fe-diluted magnetic semiconductors regarding its magnetic properties. Electrochemical texts show severe structural changes that occurred during the first charge–discharge process of the cells. The structural transformation from α-LiFeO$_2$ to LiFe$_5$O$_8$ spinel phase has been evidenced by ex situ X-ray diffraction and Raman spectroscopy [231].

5.4   Concluding Remarks

Numerous efforts are done to replace the lithium-cobalt oxide used in the first generation of commercial lithium-ion batteries by materials with low cost and environmental concerns. The development of new materials needs new synthesis procedure such as sol–gel processing, ion-exchange reaction, and hydrothermal reaction. The chemical and structural stabilities of the transition-metal oxide electrodes have been compared by studying bulk samples. In this respect, the various physicochemical techniques are welcome to design the best structure. Synthesis of amorphous compounds could help the knowledge of microstructures in this regard.

The search for layered materials that exhibit superior cycling performance has led to the study of transition-metal- and cation-substituted materials of the series LiMO$_2$ with $M =$ (Ni, Co), (Ni, Co, Al), (Ni, Mn, Co) and composite materials. Doping was successful in many cases such as LiNiO$_2$, LiCoO$_2$, and LiMnO$_2$. The LiCo$_{1-y}M_y$O$_2$ system showing relatively better chemical stability can replace the conventional LiCoO$_2$ with respect to oxygen loss. New systems such as

$LiNi_{0.5}Mn_{0.5}O_2$ and $LiNi_{0.33}Mn_{0.33}Co_{0.33}O_4$ show interesting electrochemical features but need better control of their crystal chemistry. Frameworks built with layered-rocksalt solid solution are very promising materials but the irreversible capacity loss must controlled by anionic substitution or surface modification. Some progress has been recently done with carbon-coating or aluminum doping. In view of maximizing the cell voltage and energy density, transition metal oxide hosts have emerged as the choice for cathodes [232–235]. The electrode properties of some of the 3*d* transition-metal oxides are summarized in Table 5.1. However, only 70 % of the theoretical capacity is currently delivered by the layered $LiMO_2$ oxides. The high capacity delivered by the $xLi_2MnO_3 \cdot (1-x)LiMO_2$ cathodes (>250 mAh g^{-1}) has been attributed to the electrochemical activation of the Li_2MnO_3 component within the crystal lattice but the studies of structural instabilities such as phase separation of Li_2MnO_3 should be clarified.

The future challenge is to develop cathodes with simple transition-metal layered oxides in which at least one lithium ion per transition-metal ion could be reversibly extracted/inserted while keeping the materials cost and toxicity low; such a cathode can nearly double the energy density compared to the present level. There are also possibilities to increase the capacity of cathode hosts perhaps by focusing on nanosized powders and amorphous materials. From a safety, cycle and shelf life points of view, such cathodes with a voltage lower than 4.5 V, but with a significantly increased capacity are desirable for future applications.

Table 5.1 Comparison of the electrode characteristics of some 3*d* transition-metal layered oxides

Compound	First discharge capacity (mAh g^{-1})	Average voltage (V vs. Li)	Li uptake	Energy density (Wh kg^{-1})
$Li_xV_2O_5$	420	2.25	3.0	923
$Li_{1+x}V_3O_8$	308	2.50	4.0	770
Li_xMoO_3	250	2.30	1.5	575
$Li_{1-x}CoO_2$	140	3.70	0.5	520
$Li_{1-x}NiO_2$	160	3.80	0.5	530
$Li_{1-x}Ni_{0.70}Co_{0.30}O_2$	180	3.75	0.6	675
$Li_{1-x}Ni_{0.80}Co_{0.15}Al_{0.05}O_2$	120	3.60	0.8	400
$Li_{1-x}Ni_{1/3}Mn_{1/3}Co_{1/3}O_2$	170	3.30	1.0	560
$Li_{1.2}Ni_{0.2}Mn_{0.6}O_2$	178	3.50	1.0	623
$Li_{1.17}Mn_{0.33}Co_{0.5}O_2$	254	3.50	1.0	889
$Li_{1.17}Ni_{0.125}Mn_{0.33}Co_{0.375}O_2$	265	3.50	1.0	927

References

1. Gamble FR, Osiecki JH, Cais M, Pisharody R, DiSalvo FL, Geballe TH (1971) Intercalation complexes of Lewis bases and layered sulfides: a large class of new superconductors. Science 174:493–497

2. Broadhead J, Butherus AD (1972) Rechargeable nonaqueous battery. US Patent 3,791,867. Accessed 24 July 1972

3. Mizushima K, Jones PC, Wiseman PJ, Goodenough JB (1980) Li_xCoO_2 $(0 < x < 1)$: a new cathode material for batteries of high energy density. Mater Res Bull 15:783–789

4. Julien C, Nazri GA (1994) Transport properties of lithium-intercalated MoO_3. Solid State Ionics 68:111–116

5. Crouch-Baker S, Dickens PG (1989) Qualitative bonding models for some molybdenum oxide phases. Solid State Ionics 32–33:219–227

6. Julien C (1990) Technological applications of solid state ionics. Mater Sci Eng B 6:9–15

7. Julien C, Hussain OM, El-Farh L, Balkanski M (1992) Electrochemical studies of lithium insertion in MoO_3 films. Solid State Ionics 53–56:400–404

8. Campanella L, Pistoia G (1971) MoO_3: a new electrode material for nonaqueous secondary battery applications. J Electrochem Soc 118:1905–1908

9. Besenhard JO, Heydecke J, Wudy E, Fritz HP, Foag W (1983) Characteristics of molybdenum oxide and chromium oxide cathodes in primary and secondary organic electrolyte batteries. II. Transport properties. Solid State Ionics 8:61–71

10. Goodenough JB (1990) Designing a reversible solid electrode. In: Akridge JR, Balkanski M (eds) Solid state microbatteries, NATO-ASI Series, Ser. B 217. Plenum, New York, pp 213–232

11. Yebka B, Julien C (1997) Lithium intercalation in sputtered MoO_3 films. Ionics 3:83–88

12. Nadkarni GS, Simmons JG (1970) Electrical properties of evaporated molybdenum oxide films. J Appl Phys 41:545

13. Goodenough JB (1971) Metallic oxides. Prog Solid State Chem 5:145–399

14. Julien C, Nazri GA (2001) Intercalation compounds for advanced lithium batteries. In: Nalwa HS (ed) Handbook of advanced electronic and photonic materials, vol 10. Academic Press, San Diego, pp 99–184

15. Bystrom A, Wilhelmi KA, Brotzen O (1950) Vanadium pentoxide a compound with five-coordinated vanadium atoms. Acta Chem Scand 4:1119–1130

16. Bachmann HG, Ahmed FR, Barnes WH (1961) The crystal structure of vanadium pentoxide. Z Kristallogr 115:110–116

17. Cava RJ, Santoro A, Murphy DW, Zahurak SM, Fleming RM, Marsh P, Roth RS (1986) he structure of the lithium-inserted metal oxide LiV_2O_5. J Solid State Chem 65:63–71

18. Murphy DW, Christian PA, DiSalvo FJ, Carides JN, Waszczak JV (1981) Lithium incorporation by V_6O_{13} and related vanadium (+4,+5) oxide cathode materials. J Electrochem Soc 128:2053–2060

19. Dickens PG, French SJ, Hight AT, Pye MF (1979) Phase relationship in the ambient temperature $Li_xV_2O_5$ system $(0.1 < x < 1.0)$. Mater Res Bull 14:1295–1299

20. Galy J (1992) Vanadium pentoxide and vanadium oxide bronzes – structural chemistry of single (S) and double (D) layer $M_xV_2O_5$ phases. J Solid State Chem 100:229–245

21. West K, Zachau-Christiansen B, Jacobsen T, Skaarup S (1991) Vanadium oxides as host materials for lithium and sodium intercalation. Mater Res Soc Symp Proc 210:449–460

22. Delmas C, Brethes S, Ménétrier M (1991) ω-$Li_xV_2O_5$ a new electrode material for rechargeable lithium batteries. J Power Sourc 34:113–118

23. Leger C, Bach S, Soudan P, Pereira-Ramos JP (2005) Structural and electrochemical properties of ω-$Li_xV_2O_5$ $(0.4 \leq x \leq 3)$ as rechargeable cathodic material for lithium batteries. J Electrochem Soc 152:A236–A241

24. Dickens PG, Reynolds GJ (1981) Thermodynamics and kinetics of the electrochemical insertion of lithium into tungsten. Solid State Ionics 5:351–354

25. Li WD, Xu CX, Du Y, Fang HT, Feng YJ, Zhen L (2014) Electrochemical lithium insertion behavior of β-Li$_x$V$_2$O$_5$ phases ($0 < x \leq 3$) as cathode material for secondary lithium batteries. J Electrochem Soc 161:A75–A83

26. Wadsley AD (1957) Crystal chemistry of non-stoichiometric pentavalent vanadium oxides: crystal structure of Li$_{1+x}$V$_3$O$_8$. Acta Crystallogr 10:261–267

27. Pistoia G, Panero S, Tocci M, Moshtev R, Manev V (1984) Solid solutions Li$_{1+x}$V$_3$O$_8$ as cathodes for high rate secondary Li batteries. Solid State Ionics 13:311–318

28. Pasquali M, Pistoia G, Manev V, Moshtev RV (1986) Li/Li$_{1+x}$V$_3$O$_8$ batteries. J Electrochem Soc 133:2454–2458

29. Pistoia G, Pasquali M, Tocci M, Moshtev RV, Manev V (1985) Li/Li$_{1+x}$V$_3$O$_8$ secondary batteries. III. Further characterization of the mechanism of Li$^+$ insertion and of the cycling behavior. J Electrochem Soc 132:281–284

30. Besenhard JO, Schöllhorn R (1976/1977) The discharge reaction mechanism of the MoO3 electrode in organic electrolytes. J Power Sourc 1:267–276

31. Schöllhorn R, Klein-Reesink F, Reimold R (1979) Formation, structure and topotactic exchange reactions of the layered hydrogen bronze H$_x$V$_3$O$_8$. J Chem Soc Chem Commun 398–399

32. Nassau K, Murphy DW (1981) The quenching and electrochemical behaviour of Li$_2$O-V$_2$O$_5$ glasses. J Non Cryst Solids 44:297–304

33. West K, Zachau-Christiansen B, Skaarup S, Saidi Y, Barker L, Olsen II, Pynenburg R, Koksbang R (1996) Comparison of LiV$_3$O$_8$ cathode materials prepared by different methods. J Electrochem Soc 143:820–826

34. Winter M, Besenhard JO, Sparhr ME, Novak P (1998) Insertion electrode materials for rechargeable lithium batteries. Adv Mater 10:725–763

35. Pistoia G, Li L, Wang G (1992) Direct comparison of cathode materials of interest for secondary high-rate lithium cells. Electrochim Acta 37:63–68

36. Kawakita J, Miura T, Kishi T (1999) Lithium insertion and extraction kinetics of Li$_{1+x}$V$_3$O$_8$. J Power Sourc 83:79–83

37. Jouanneau S, Verbaere A, Lascaud S, Guyomard D (2006) Improvement of the lithium insertion properties of Li$_{1.1}$V$_3$O$_8$. Solid State Ionics 177:311–315

38. Jouanneau S, Le Gal La Salle A, Verbaere A, Guyomard D (2005) The origin of capacity fading upon lithium cycling in Li$_{1.1}$V$_3$O$_8$. J Electrochem Soc 152:A1660–A1667

39. Xie JG, Li JX, Zhan H, Zhou YH (2003) Low-temperature sol-gel synthesis of Li$_{1.2}$V$_3$O$_8$ from V$_2$O$_5$ gel. Mater Lett 57:2682–2687

40. Kawakita J, Katayama Y, Miura T, Kishi T (1998) Lithium insertion behavior of Li$_{1+x}$V$_3$O$_8$ prepared by precipitation technique in CH$_3$OH. Solid State Ionics 110:199–207

41. Liu HM, Wang YG, Wang KX, Wang YR, Zhou HS (2009) Synthesis and electrochemical properties of single-crystalline LiV$_3$O$_8$ nanorods as cathode materials for rechargeable lithium batteries. J Power Sourc 192:668–673

42. Liu HM, Wang YG, Wang WS, Zhou HS (2011) A large capacity of LiV$_3$O$_8$ cathode material for rechargeable lithium-based batteries. Electrochim Acta 56:1392–1398

43. Si YC, Jiao LF, Yan HT, Li HX, Wang YM (2009) Structural and electrochemical properties of LiV$_3$O$_8$ prepared by combustion synthesis. J Alloys Compd 486:400–405

44. Ju SH, Kang YC (2010) Morphological and electrochemical properties of LiV$_3$O$_8$ cathode powders prepared by spray pyrolysis. Electrochim Acta 55:6088–6092

45. Sakunthala A, Reddy MV, Selvasekarapandian S, Chowdari BVR, Selvin PC (2010) Preparation, characterization and electrochemical performance of lithium trivanadate rods by a surfactant-assisted olymer precursor method for lithium batteries. J Phys Chem C 114:8099–8107

46. Hui Y, Juan L, Zhang JG, Jia DZ (2007) Synthesis and properties of LiV$_3$O$_8$ nanomaterials as the cathode material for Li-ion battery. J Inorg Mater 22:447–450

47. Yang H, Li J, Zhang XG, Jin YL (2008) Synthesis of LiV$_3$O$_8$ nanocrystallites as cathode materials for lithium ion batteries. J Mater Process Technol 207:265–270

48. Liu XH, Wang JQ, Zhang JY, Yang SR (2007) Sol-gel template synthesis of LiV_3O_8 nanowires. J Mater Sci 42:867–871
49. Lee KP, Manesh KM, Kim KS, Gopalan AY (2009) Synthesis and characterization of nanostructured wires (1D) to plates (3D) LiV_3O_8 combining sol-gel and electrospinning processes. J Nanosci Nanotechnol 9:417–422
50. Xu HY, Wang H, Song ZQ, Wang YW, Yan H, Yoshimura M (2004) Novel chemical method for synthesis of LiV_3O_8 nanorods as cathode materials for lithium ion batteries. Electrochim Acta 49:349–353
51. Sun D, Jin G, Wang H, Huang X, Ren Y, Jiang J, He H, Tang Y (2014) $Li_xV_2O_5/LiV_3O_8$ nanoflakes with significantly improved electrochemical performance for Li-ion batteries. J Mater Chem A 2:8009–8016
52. Liu L, Jiao LF, Sun JL, Zhang YH, Zhao M, Yuan HT, Wang YM (2008) Electrochemical performance of $LiV_{3-x}Ni_xO_8$ cathode materials synthesized by a novel low-temperature solid-state method. Electrochim Acta 53:7321–7325
53. Wang H, Ren Y, Wang Y, Wang W, Liu S (2012) Synthesis of LiV_3O_8 nanosheets as a high-rate cathode material for rechargeable lithium batteries. Cryst Eng Comm 14:2831–2836
54. Feng CQ, Chew SY, Guo ZP, Wang JZ, Liu HK (2007) An investigation of polypyrrole-LiV_3O_8 composite cathode materials for lithium-ion batteries. J Power Sourc 174:1095–1099
55. Kumagai N, Yu A (1997) Ultrasonically treated LiV_3O_8 as a cathode material for secondary lithium batteries. J Electrochem Soc 144:830–835
56. Orman HJ, Wiseman PJ (1984) Cobalt(III) lithium oxide, $CoLiO_2$: structure refinement by powder neutron diffraction. Acta Crystallogr C 40:12–14
57. Delmas C, Fouassier C, Hagenmuller P (1980) Structural classification and properties of the layered oxides. Physica B 99:81–85
58. Venkatraman S, Manthiram A (2002) Synthesis and characterization of P3-type $CoO_{2-\delta}$. Chem Mater 14:3907–3912
59. Gao Y, Yakovleva MV, Ebner WB (1998) Novel $LiNi_{1-x}Ti_{x/2}Mg_{x/2}O_2$ compounds as cathode materials for safer lithium-ion batteries. Electrochem Solid State Lett 1:117–119
60. Cho J, Kim G, Lim HS (1999) Effect of preparation methods of $LiNi_{1-x}Co_xO_2$ cathode materials on their chemical structure of electrode performance. J Electrochem Soc 146:3571–3576
61. Mueller-Neuhaus JR, Dunlap RA, Dahn JR (2000) Understanding irreversible capacity in $LiNi_{1-y}Fe_yO_2$ cathode materials. J Electrochem Soc 147:3598–3605
62. Goodenough JB, Mizuchima K (1981) Electrochemical cell with new fast ion conductors. US Patent 4,302,518. Accessed 24 Nov 1981
63. Nagaura T, Tozawa K (1990) Lithium ion rechargeable battery. Prog Batteries Solar Cells 9:209–212
64. Gummow RJ, Thackeray MM, David WIF, Hull S (1992) Structure and electrochemistry of lithium cobalt oxide synthesized at 400 °C. Mater Res Bull 27:327–337
65. Shao-Horn Y, Hackney SA, Kahaian AJ, Thackeray MM (2002) Structural stability of $LiCoO_2$ at 400 °C. J Solid State Chem 168:60–68
66. Johnston WD, Heikes RR, Sestrich D (1958) The preparation, crystallography and magnetic properties of the $Li_xCo_{(1-x)}O$ system. J Phys Chem Solids 7:1–13
67. Ohzuku T, Ueda A (1994) Solid-state redox reactions of $LiCoO_2$ (R-3 m) for 4 volt secondary lithium cells. J Electrochem Soc 141:2972–2977
68. Oh IH, Hong YS, Sun YK (1997) Low-temperature preparation of ultrafine $LiCoO_2$ powders by the sol-gel method. J Mater Sci 32:3177–3182
69. Julien C, El-Farh L, Rangan S, Massot M (1999) Synthesis of $LiNi_{1-y}Co_yO_2$ cathode materials prepared by a citric acid-assisted sol-gel method for lithium batteries. J Sol Gel Sci Technol 15:63–72
70. Santiago EI, Andrade AVC, Paiva-Santos CO, Bulhoes LOS (2003) Structural and electro-chemical properties of $LiCoO_2$ prepared by combustion synthesis. Solid State Ionics 158:91–102

71. Han CH, Hong YS, Park CM, Kim K (2001) Synthesis and electrochemical properties of lithium cobalt oxides prepared by molten-salt synthesis using the eutectic mixture of LiCl-Li_2CO_3. J Power Sourc 92:95–101

72. Kosova NV, Anufrienko VF, Larina TV, Rougier A, Aymard L, Tarascon JM (2002) Disordering and electronic state of cobalt ions in mechanochemically synthesized $LiCoO_2$. J Solid State Chem 165:56–64

73. Brylev OA, Shlyakhtin OA, Kulova TL, Skundin AM, Tretyakov YD (2003) Influence of chemical prehistory on the phase formation and electrochemical performance of $LiCoO_2$ materials. Solid State Ionics 156:291–299

74. Larcher D, Palacin MR, Amatucci GG, Tarascon JM (1997) Electrochemically active $LiCoO_2$ and $LiNiO_2$ made by cationic exchange under hydrothermal conditions. J Electrochem Soc 144:408–417

75. Yan H, Huang X, Zhonghua L, Huang H, Xue R, Chen L (1997) Microwave synthesis of $LiCoO_2$ cathode materials. J Power Sourc 68:530–532

76. Akimoto J, Gotoh Y, Oosawa Y (1998) Synthesis and structure refinement of $LiCoO_2$ single crystals. J Solid State Chem 141:298–302

77. Amatucci GG, Tarascon JM, Klein LC (1996) CoO_2, the end member of the Li_xCoO_2 solid solution. J Electrochem Soc 143:1114–1123

78. Chebiam RV, Prado F, Manthiram A (2001) Soft chemistry synthesis and characterization of layered $Li_{1-x}Ni_{1-y}Co_yO_{2-\delta}$ ($0 \leq x \leq 1$ and $0 \leq y \leq 1$). Chem Mater 13:2951–2957

79. Chebiam RV, Kannan AM, Prado F, Manthiram A (2001) Comparison of the chemical stability of the high energy density cathodes of lithium-ion batteries. Electrochem Commun 3:624–627

80. Delmas C, Saadoune I (1992) Electrochemical and physical properties of the $Li_xNi_{1-y}Co_yO_2$ phases. Solid State Ionics 53–56:370–375

81. Venkatraman S, Shin Y, Manthiram A (2003) Phase relationships and structural and chemical stabilities of charged $Li_{1-x}CoO_{2-\delta}$ and $Li_{1-x}Ni_{0.85}Co_{0.15}O_{2-\delta}$ cathodes. Electrochem Solid State Lett 6:A9–A12

82. Reimers JN, Dahn JR (1992) Electrochemical and in situ X-ray diffraction studies of lithium intercalation in Li_xCoO_2. J Electrochem Soc 139:2091–2097

83. Mauger A, Julien CM (2014) Surface modifications of electrode materials for lithium-ion batteries: status and trends. Ionics 20:751–787

84. Laubach S, Laubach S, Schmidt C, Ensling D, Schmid S, Jaegermann W, Thissen A, Nikolowski K, Erhenberg H (2009) Changes in the crystal end electronic structure of $LiCoO_2$ and $LiNiO_2$ upon Li intercalation and de-intercalation. Phys Chem Chem Phys 11:3278–3289

85. Hirano A, Kanno R, Kawamoto Y, Takeda Y, Yamamura K, Takano M, Ohyama K, Ohashi M, Yamaguchi Y (1995) Relationship between non-stoichiometry and physical properties in $LiNiO_2$. Solid State Ionics 78:123–131

86. Ohzuku T, Ueda A, Nagayama M, Iwakashi Y, Komori H (1993) Comparative study of $LiCoO_2$, $LiNi_{1/2}Co_{1/2}O_2$ and $LiNiO_2$ for 4 volt secondary lithium cells. Electrochim Acta 38:1159–1167

87. Dahn JR, Fuller EW, Obrovac M, von Sacken U (1994) Thermal stability of Li_xCoO_2, Li_xNiO_2 and λ-MnO_2 and consequence for the safety of Li-ion cells. Solid State Ionics 69:265–270

88. Zhang Z, Fouchard D, Rea JR (1998) Differential scanning calorimetry material studies: implications for the safety of lithium-ion cells. J Power Sourc 70:16–20

89. Bianchi V, Caurant D, Baffier N, Belhomme C, Chappel E, Chouteau G, Bach S, Pereira-Ramos JP, Sulpice A, Wilmann P (2001) Synthesis, structural characterization and magnetic properties of quasistoichiometric $LiNiO_2$. Solid State Ionics 140:1–17

90. Arai H, Okada S, Yamaki J (1998) Thermal behavior of $Li_{1-y}NiO_2$ and the decomposition mechanism. Solid State Ionics 109:295–302

91. Li W, Curie J (1997) Morphology effects on the electrochemical performance of LiNi$_{1-x}$Co$_x$O$_2$. J Electrochem Soc 144:2773–2779

92. Guilmard M, Pouillerie C, Croguennec L, Delmas C (2003) Structural and electrochemical properties of LiNi$_{0.70}$Co$_{0.15}$Al$_{0.15}$O$_2$. Solid State Ionics 160:39–50

93. Ohzuku T, Ueda A, Kouguchi M (1995) Synthesis and characterization of LiAl$_{1/4}$Ni$_{3/4}$O$_2$ (R-3 m) for lithium-ion (shuttlecock) batteries. J Electrochem Soc 142:4033–4039

94. Delmas C, Saadoune I, Rougier A (1993) The cycling properties of the Li$_x$Ni$_{1-y}$Co$_y$O$_2$ electrode. J Power Sourc 44:595–602

95. Kannan AM, Manthiram A (2002) Degradation of LiNi$_{0.8}$Co$_{0.2}$O$_2$ cathode surfaces in high-power lithium-ion batteries. Electrochem Solid State Lett 5:A164–A166

96. Gummow RJ, Thackeray MM (1993) Characterization of LT-Li$_x$Co$_{1-y}$Ni$_y$O$_2$ electrodes for rechargeable lithium cells. J Electrochem Soc 140:3365–3368

97. Julien C, Letranchant C, Rangan S, Lemal M, Ziolkiewicz S, Castro-Garcia S, El-Farh L, Benkaddour M (2000) Layered LiNi$_{0.5}$Co$_{0.5}$O$_2$ cathode materials grown by soft-chemistry via various solution methods. Mater Sci Eng B 76:145–155

98. Ohzuku T, Yanagawa T, Kouguchi M, Ueda A (1997) Innovative insertion material of LiAl$_{1/4}$Ni$_{3/4}$O$_2$ (R-3 m) for lithium-ion (shuttlecock) batteries. J Power Sourc 68:131–134

99. Julien C, Nazri GA, Rougier A (2000) Electrochemical performances of layered LiM$_{1-y}$M$_y$'O$_2$ (M = Ni, Co; M' = Mg, Al, B) oxides in lithium batteries. Solid State Ionics 135:121–130

100. Julien C, Michael SS, Ziolkiewicz S (1999) Structural and electrochemical properties of LiNi$_{0.3}$Co$_{0.7}$O$_2$ synthesized by different low-temperature techniques. Int J Inorg Mat 1:29–34

101. Abdel-Ghany AE, Hashem AMA, Abuzeid HAM, Eid AE, Bayoumi HA, Julien CM (2009) Synthesis, structure characterization and magnetic properties of nanosized LiCo$_{1-y}$Ni$_y$O$_2$ prepared by sol-gel citric acid route. Ionics 15:49–59

102. Goodenough JB (1999) Oxide engineering for advanced power sources. Electrochem Soc Proc 99–24:1–14

103. Julien C (2000) Local cationic environment in lithium nickel-cobalt oxides used as cathode materials for lithium batteries. Solid State Ionics 136–137:887–896

104. Senaris-Rodriguez MA, Castro-Garcia S, Castro-Couceiro A, Julien C, Hueso LE, Rivas J (2003) Magnetic clusters in LiNi$_{1-y}$Co$_y$O$_2$ nanomaterials used as cathodes in lithium-ion batteries. Nanotechnology 14:277–282

105. Zhang X, Julien CM, Mauger A, Gendron F (2011) Magnetic analysis of lamellar oxides for Li-ions batteries. Solid State Ionics 188:148–155

106. Delmas C, Ménétrier M, Croguennec L, Saadoune I, Rougier A, Pouillerie C, Prado G, Grüne M, Fournès L (1999) An overview of the Li(Ni, M)O2 systems: synthesis, structure and properties. Electrochim Acta 45:243–253

107. Caurant D, Baffier N, Bianchi V, Grégoire G, Bach S (1996) Preparation by a chimie douce route and characterization of LiNi$_z$Mn$_{1-z}$O$_2$ (0.5 ≤ z ≤ 1) cathode materials. J Mater Chem 6:1149–1155

108. Julien C, Castro-Garcia S (2001) Lithiated cobaltates for Li-ion batteries. Structure, morphology and electrochemistry of oxides grown by solid-state reaction, wet chemistry and film deposition. J Power Sourc 97–98:290–293

109. Ramana CV, Zaghib K, Julien CM (2006) Highly oriented growth of pulsed-laser deposited LiNi$_{0.8}$Co$_{0.2}$O$_2$ films for application in microbatteries. Chem Mater 18:1397–1400

110. Julien C (2000) Structure, morphology and electrochemistry of doped lithium cobalt oxides. Ionics 6:451–460

111. Julien C (2003) Local structure and electrochemistry of lithium cobalt oxides and their doped compounds. Solid State Ionics 157:57–71

112. Julien C, Camacho-Lopez MA, Lemal M, Ziolkiewicz S (2002) LiCo$_{1-y}$M$_y$O$_2$ positive electrodes for rechargeable lithium batteries. I. Aluminium doped materials. Mater Sci Eng B 95:6–13

113. Amdouni N, Zarrouk H, Soulette F, Julien C (2003) $LiAl_yCo_{1-y}O_2$ ($0.0 \leq y \leq 0.3$) intercalation compounds synthesized from the citrate precursors. Mater Chem Phys 80:205–214

114. Julien CM, Mauger A, Groult H, Zhang X, Gendron F (2011) $LiCo_{1-y}B_yO_2$ as cathode materials for rechargeable lithium batteries. Chem Mater 23:208–218

115. Amdouni N, Zarrouk H, Julien C (2003) Low temperature synthesis of $LiCr_{0.3}Co_{0.7}O_2$ intercalation compounds using citrate, oxalate, succinate and glycinate precursors. British Ceram Trans 102:27–30

116. Julien C, Letranchant C, Lemal M, Ziolkiewicz S, Castro-Garcia S (2002) Layered $LiNi_{1-y}Co_yO_2$ compounds synthesized by a glycine-assisted combustion method for lithium batteries. J Mater Sci 37:2367–2375

117. Mazas-Brandariz D, Senaris-Rodriguez MA, Castro-Garcia S, Camacho-Lopez MA, Julien C (1999) Structural properties of $LiNi_{1-y}Co_yO_2$ ($0 \leq y \leq 1$) synthesized by wet chemistry via malic acid-assisted technique. Ionics 5:345–350

118. Castro-Couceiro A, Castro-Garcia S, Senaris-Rodriguez MA, Soulette F, Julien C (2002) Effects of the aluminum doping on the microstructure and morphology of $LiNi_{0.5}Co_{0.5}O_2$ oxides. Ionics 8:192–200

119. Abuzeid HA, Hashem AM, Abdel-Ghany AE, Eid AE, Mauger A, Groult H, Julien CM (2011) Study of the delithiation of $LiMn_{0.2}Co_{0.8}O_2$ cathode material for lithium batteries. ECS Trans 35–34:95–102

120. Abuzeid HAM, Hashem AMA, Abdel-Ghany AE, Eid AE, Mauger A, Groult H, Julien CM (2011) De-intercalation of $LiCo_{0.8}Mn_{0.2}O_2$: a magnetic approach. J Power Sourc 196:6440–6448

121. Wang GX, Bewlay S, Yao J (2003) Multiple-ion doped lithium nickel oxides as cathode materials for lithium-ion batteries. J Power Sourc 119–121:189–194

122. Kostecki R, McLarnon F (2004) Local-probe studies of degradation of composite $LiNi_{0.80}Co_{0.15}Al_{0.05}O_2$ cathodes in high-power lithium-ion cells. Electrochem Solid State Lett 7:A380–A383

123. Weaving J, Coowar F, Teagle D, Cullen J, Dass V, Bindin P, Green R, Macklin W (2001) Development of high energy density Li-ion batteries based on $LiNi_{1-x-y}Co_xAl_yO_2$. J Power Sourc 97:733–735

124. Bang HJ, Joachin H, Yang H, Amine K, Prakash J (2006) Contribution of the structural changes of $LiNi_{0.80}Co_{0.15}Al_{0.05}O_2$ cathodes on the exothermic reactions in Li-ion cells. J Electrochem Soc 153:A731–A737

125. Ju S, Jang H, Kang Y (2007) Al-doped Ni-rich cathode powders prepared from the precursor powders with fine size and spherical shape. Electrochim Acta 52:7286–7292

126. Biensan P, Simon B, Pérès JP, de Guilbert A, Broussely M, Bodet JM, Perton F (1999) On safety of lithium-ion cells. J Power Sourc 81:906–912

127. Majumdar SB, Nieto S, Katiyar RS (2006) Synthesis and electrochemical properties of $LiNi_{0.80}(Co_{0.20-x}Al_x)O_2$ ($x = 0.0$ and 0.05) cathodes for Li ion rechargeable batteries. J Power Sourc 154:262–267

128. Chebiam RV, Prado F, Manthiram A (2001) Structural instability of delithiated $Li_{1-x}Ni_{1-y}Co_yO_2$ cathodes. J Electrochem Soc 148:A49–A53

129. Cho Y, Cho J (2010) Significant improvement of $LiNi_{0.80}Co_{0.15}Al_{0.05}O_2$ cathodes at 60 °C by SiO_2 dry coating for Li-ion batteries. J Electrochem Soc 157:A625–A629

130. Cho Y, Lee YS, Park SA, Lee Y, Cho J (2010) $LiNi_{0.80}Co_{0.15}Al_{0.05}O_2$ cathodes materials prepared by TiO_2 nanoparticle coatings on $Ni_{0.80}Co_{0.15}Al_{0.05}(OH)_2$ precursors. Electrochim Acta 56:333–339

131. Lee DJ, Scrosati B, Sun YK (2011) $Ni_3(PO_4)_2$-coated $Li(Ni_{0.80}Co_{0.15}Al_{0.05})O_2$ lithium battery electrode with improved cycling performance at 55 °C. J Power Sourc 196:7742–7746

132. Lee SH, Yoon CS, Amine K, Sun YK (2013) Improvement of long-term cycling performance of $Li(Ni_{0.80}Co_{0.15}Al_{0.05})O_2$ by AlF_3 coating. J Power Sourc 234:201–207

133. Lim SN, Ahn W, Yeon SH, Park SB (2014) Enhanced elevated-temperature performance of $LiNi_{0.80}Co_{0.15}Al_{0.05}O_2$ electrodes coated with Li_2O-$2B_2O_3$ glass. Electrochim Acta 136:1–9

134. Ju JH, Chung YM, Bak YR, Hwang MJ, Ryu KS (2010) The effects of carbon nano-coating on $Li(Ni_{0.80}Co_{0.15}Al_{0.05})O_2$ cathode material using organic carbon for Li-ion battery. Surf Rev Lett 17:51–58

135. Belharouak I, Lu W, Vissers D, Amine K (2006) Safety characteristics of Li $(Ni_{0.8}Co_{0.15}Al_{0.05})O_2$ and $Li(Ni_{1/3}Co_{1/3}Mn_{1/3})O_2$. Electrochem Commun 8:329–335

136. Ohzuku T, Makimura Y (2001) Layered lithium insertion material of $LiNi_{1/2}Mn_{1/2}O_2$: a possible alternative to $LiCoO_2$ for advanced lithium-ion batteries. Chem Lett 30:744–745

137. Liu Y, Chen B, Cao F, Zhao X, Yuan J (2011) Synthesis of nanoarchitectured $LiNi_{0.5}Mn_{0.5}O_2$ spheres for high-performance rechargeable lithium-ion batteries via an in situ conversion route. J Mater Chem 21:10437–10441

138. Abdel-Ghany A, Zaghib K, Gendron F, Mauger A, Julien CM (2007) Structural, magnetic and electrochemical properties of $LiNi_{0.5}Mn_{0.5}O_2$ as positive electrode for Li-ion batteries. Electrochim Acta 52:4092–4100

139. Yamaura K, Takano M, Hirano A, Kanno R (1996) Magnetic properties of $Li_{1-x}Ni_{1+x}O_2$ $(0 \leq x \leq 0.08)$. J Solid State Chem 127:109–118

140. Goodenough JB (1963) Magnetism and the chemical bond. Wiley-Interscience, New York

141. Liu Z, Yu A, Lee JY (1999) Synthesis and characterization of $LiNi_{1-x-y}Co_yMn_yO_2$ as the cathode materials secondary lithium batteries. J Power Sourc 81–82:416–419

142. Lu Z, MacNeil DD, Dahn JR (2001) Layred $Li[Ni_xCo_{1-2x}Mn_x]O_2$ cathode materials for lithium-ion batterie. Electrochem Solid State Lett 4:A200–A203

143. MacNeil DD, Lu Z, Dahn JR (2002) Structure and electrochemistry of $Li[Ni_xCo_{1-2x}Mn_x]O_2$ $(0 \leq x \leq 1/2)$. J Electrochem Soc 149:A1332–A1336

144. Shaju KM, Subba-Rao GV, Chowdari BVR (2002) Performance of layered $Li(Ni_{1/3}Co_{1/3}Mn_{1/3})O_2$ as cathode for Li-ion batteries. Electrochim Acta 48:145–151

145. Yabuuchi N, Ohzuku T (2003) Novel lithium insertion material of $Li Ni_{1/3}Co_{1/3}Mn_{1/3}O_2$ for advanced lithium-ion batteries. J Power Sourc 119–121:171–174

146. Lee S, Park SS (2012) Atomistic simulation study of mixed-metal oxide $(LiNi_{1/3}Mn_{1/3}Co_{1/3}O_2)$ cathode material for lithium ion battery. J Phys Chem C 116:6484–6489

147. Wang L, Li J, He X, Pu W, Wan C, Jiang C (2005) Recent advances in layered $LiNi_xCo_yMn_{1-x-y}O_2$ cathode materials for lithium ion batteries. J Solid State Electrochem 13:1157–1164

148. Fergus JW (2010) Recent developments in cathode materials for lithium ion batteries. J Power Sourc 195:939–954

149. Zhu JP, Xu QB, Yang HW, Zhao JJ, Yang G (2011) Recent development of $LiNi_{1/3}Co_{1/3}Mn_{1/3}O_2$ as cathode material of lithium ion battery. J Nanosci Nanotechnol 11:10357–10368

150. Zeng D, Cabana J, Bréger J, Yoon WS, Grey CP (2007) Cation ordering in $Li[Ni_xMn_xCo_{(1-2x)}]O_2$-layered cathode materials. Chem Mater 19:6277–6289

151. Liao PY, Duh JG, Sheen SR (2005) Microstructure and electrochemical performance of $LiNi_{0.6}Co_{0.4-x}Mn_xO_2$ cathode materials. J Power Sourc 143:212–218

152. Gan CL, Hu XH, Zhan H (2005) Synthesis and characterization of $Li_{1.2}Ni_{0.6}Co_{0.2}Mn_{0.2}O_{2+\delta}$ as cathode material for secondary lithium batteries. Solid State Ionics 176:687–692

153. Lee JW, Lee JH, Tan-Viet T, Lee JY, Kim JS, Lee CH (2010) Synthesis of $LiNi_{1/3}Mn_{1/3}Co_{1/3}O_2$ cathode materials by using a supercritical water method in a bath reactor. Electrochim Acta 55:3015–3021

154. Na SH, Kim HS, Moon SI (2005) The effect of Si doping on the electrochemical characteristics of $LiNi_xMn_yCo_{(1-x-y)}O_2$. Solid State Ionics 176:313–317

155. Ohzuku T, Makimura Y (2001) Layered lithium insertion material $LiNi_{1/3}Mn_{1/3}Co_{1/3}O_2$ for lithium-ion batteries. Chem Lett 30:642–643

156. Ngala JK, Chernova NA, Ma M, Mamak M, Zavalij PY, Whittingham MS (2004) The synthesis, characterization and electrochemical behavior of the layered $LiNi_{0.4}Mn_{0.4}Co_{0.2}O_2$ compound. J Mater Chem 14:214–220
157. Lee MH, Kang YJ, Myung ST, Sun YK (2004) Synthetic optimization of $Li[Ni_{1/3}Mn_{1/3}Co_{1/3}]O_2$ via co-precipitation. Electrochim Acta 50:939–948
158. Oh SW, Park SH, Park CW, Sun YK (2004) Structural and electrochemical properties of layered $Li(Ni_{0.5}Mn_{0.5})_{1-x}Co_xO_2$ positive materials synthesized by ultrasonic spray pyrolysis method. Solid State Ionics 171:167–172
159. Li DC, Noguchi H, Yoshio M (2004) Electrochemical characteristics of $LiNi_{0.5-x}Mn_{0.5-x}Co_{2x}O_2$ ($0 \leq x \leq 0.1$) prepared by spray dry method. Electrochim Acta 50:427–430
160. Wen JW, Liu J, Wu H, Chen CH (2007) Synthesis and electrochemical characterization of $LiCo_{1/3}Ni_{1/3}Mn_{1/3}O_2$ by radiated polymer gel method. J Mater Sci 42:7696–7701
161. Ren H, Li X, Peng Z (2011) Electrochemical properties of $Li[Ni_{1/3}Mn_{1/3}Al_{1/3-x}Co_x]O_2$ as a catode material for litium ion battery. Electrochim Acta 56:7088–7091
162. Du K, Peng Z, Hu G, Yang Y, Qi L (2009) Synthesis of $LiMn_{1/3}Ni_{1/3}Co_{1/3}O_2$ in molten KCl for rechargeable lithium-ion batteries. J Alloy Comp 476:329–334
163. Sinha NN, Munichandriaah N (2010) High rate capability of porous $LiNi_{1/3}Mn_{1/3}Co_{1/3}O_2$ synthesized by polymer template route. J Electrochem Soc 157:A647–A653
164. Samarasingh P, Tran-Nguyen DH, Behm M, Wijayasinghe A (2008) $LiNi_{1/3}Mn_{1/3}Co_{1/3}O_2$ synthesized by the Pechini method for the positive electrode in Li-ion batteries: material characteristics and electrochemical behaviour. Electrochim Acta 53:7995–8000
165. Fujii Y, Miura H, Suzuki N, Shoji T, Nakayama N (2007) Structural and electrochemical properties of $LiNi_{1/3}Co_{1/3}Mn_{1/3}O_2$: calcinations temperature dependence. J Power Sourc 171:894–903
166. Park SH, Oh SW, Sun YK (2005) Synthesis and structural characterization of layered $Li[Li_{1/3+x}Co_{1/3}Mn_{1/3-2x}Mo_x]O_2$ cathode materials by ultrasonic spray pyrolysis. J Power Sourc 146:622–625
167. Li DC, Sasaki Y, Kobayakawa K (2006) Morphological, structural and electrochemical characteristics of $LiNi_{0.5}Mn_{0.4}M_{0.1}O_2$ ($M = Li$, Mg, Co, Al). J Power Sourc 157:488–493
168. Kim GH, Kim JH, Myung ST (2005) Improvement of high-voltage cycling behavior of surface-modified $Li[Ni_{1/3}Co_{1/3}Mn_{1/3}]O_2$ cathodes by fluorine substitution for Li-ion batteries. J Electrochem Soc 152:A1707–A1713
169. Ben-Kamel K, Amdouni N, Abdel-Ghany A, Zaghib K, Mauger A, Gendron F, Julien CM (2008) Local structure and electrochemistry of $LiNi_yMn_yCo_{1-2y}O_2$ electrode materials for Li-ion batteries. Ionics 14:89–97
170. Aurbach D, Gamolsky K, Markovsky B, Salitra G, Gofer GY, Heider U, Oesten R, Schmidt M (2000) The study of surface phenomena related to the electrochemical intercalation into Li_xMO_y host materials ($M = Ni$, Mn). J Electrochem Soc 147:1322–1331
171. Lee EH, Park JH, Cho JH, Cho SJ, Kim DW, Dan H, Kang Y, Lee SY (2013) Direct ultra-violet-assisted conformal coating of nanometer-thick poly(tri(2-(acryloyloxy)ethyl) phosphate gel polymer electrolytes on high-voltage $LiNi_{1/3}Co_{1/3}Mn_{1/3}O_2$ cathodes. J Power Sourc 244:389–394
172. Choi J, Manthiram A (2004) Comparison of the electrochemical behaviours of stoichiometric $Li_{1.03}(Ni_{1/3}Mn_{1/3}Co_{1/3})_{0.97}O_2$ and lithium excess $LiNi_{1/3}Mn_{1/3}Co_{1/3}O_2$. Electrochem Solid State Lett 7:A365–A368
173. Zhang X, Jiang WJ, Mauger A, Qi L, Gendron F, Julien CM (2010) Minimization of the cation mixing in $Li_{1+x}(NMC)_{1-x}Co_{1/3}O_2$ as cathode material. J Power Sourc 195:1292–1301
174. Ligneel E, Nazri GA (2009) Improvement of $LiNi_{1/3}Mn_{1/3}Co_{1/3}O_2$ by a cationic substitution and effect of over-lithiation. ECS Trans 16–50:21–29
175. Robertson AD, Bruce PG (2003) Mechanism of electrochemical activity in Li_2MnO_3. Chem Mater 15:1984–1992
176. Gan C, Zhan H, Hu X, Zhou Y (2005) Origin of the irreversible plateau (4.5 V) of $Li[Li_{0.182}Ni_{0.182}Co_{0.091}Mn_{0.545}]O_2$ layered material (2005). Electrochem Commun 7:1318–1322

177. Lei CH, Wen JG, Sardela M, Bareno J, Petrov I, Kang SH, Abraham DP (2009) Structural study of Li_2MnO_3 by electron microscopy. J Mater Sci 44:5579–5587

178. Yu DYW, Yanagida K, Kato Y, Nakamura H (2009) Electrochemical activities in Li_2MnO_3 batteries and energy storage. J Electrochem Soc 156:A417–A424

179. Amalraj F, Markovsky B, Sharon D, Talianker M, Zinigrad E, Persky R, Haik O, Grinblat J, Lampert J, Schulz-Dobrick M, Garsuch A, Burlaka L, Aurbach D (2012) Study of the electrochemical behavior of the "inactive" Li_2MnO_3. Electrochim Acta 78:32–39

180. Julien CM, Massot M (2003) Lattice vibrations of materials for lithium rechargeable batteries III. Lithium manganese oxides. Mater Sci Eng B 100:69–78

181. Johnson CS, Li N, Lefief C, Vaughey JT, Thackeray MM (2008) Synthesis, characterization and electrochemistry of lithium battery electrodes: xLi_2MnO_3-(1-x)$LiMn_{0.333}Ni_{0.333}Co_{0.333}O_2$ ($0 \leq x \leq 0.7$). Chem Mater 20:6095–6106

182. Lu ZH, Dahn JR (2002) Understanding the anomalous capacity of $Li/Li[Ni_xLi_{(1/3-2x/3)}Mn_{(2/3-x/3)}]O_2$ cells using in situ X-ray diffraction and electrochemical studies. J Electrochem Soc 149:A815–A822

183. Armstrong AR, Robertson AD, Bruce PG (2005) Overcharging manganese oxides: extracting lithium beyond Mn^{4+}. J Power Sourc 146:275–280

184. Okamoto Y (2012) Ambivalent effect of oxygen vacancies on Li_2MnO_3: a first principles study. J Electrochem Soc 159:A152–A157

185. Gabrisch H, Yi T, Yazami R (2008) Transmission electron microscope studies of $LiNi_{1/3}Mn_{1/3}Co_{1/3}O_2$ before and after long-term aging at 70 °C. Electrochem Solid State Lett 11:A119–A124

186. Meng YS, de Dompablo EA (2009) First principles computational materials design for energy storage materials in lithium ion batteries. Energy Environ Sci 2:589–609

187. Ito A, Shoda K, Sato Y, Hatano M, Horie H, Ohsawa Y (2011) Direct observation of the partial formation of a framework structure for Li-rich layered cathode material $Li[Ni_{0.17}Li_{0.2}Co_{0.17}Mn_{0.56}]O_2$ upon the first charge and discharge. J Power Sourc 196:4785–4790

188. Amalraj F, Talianker M, Markovsky B, Sharon D, Burlaka L, Shafir G, Zinigrad E, Haik O, Aurbach D, Lampert J, Schulz-Dobrick M, Garsuch A (2013) Studies of Li and Mn-rich $Li_x[MnNoCo]O_2$ electrodes: electrochemical performance, structure, and the effect of the aluminum fluoride coating. J Electrochem Soc 160:A2220–A2233

189. Amalraj SF, Burlaka L, Julien CM, Mauger A, Kovacheva D, Talianker M, Markovsky B, Auirbach D (2014) Phase transitions in Li_2MnO_3 electrodes at various states-of-charge. Electrochim Acta 123:395–404

190. Von Meyer G, Hoppe R (1976) ZuV thermischen verhalten von Li_3MnO_4. Uber α- und β-Li_2MnO_3. Z Anorg Allg Chem 424:257–261

191. Jonson CS, Kim JS, Lefief C, Li N, Vaughey JT, Thackeray MM (2004) The significance of the Li_2MnO_3 component in composite xLi_2MnO_3·(1-x)$LiMn_{0.5}Ni_{0.5}O_2$ electrodes. Electrochem Commun 6:1085–1091

192. Thackeray MM, Kang SH, Johnson CS, Vaughey JT, Hackney SA (2006) Comments on the structural complexity of lithium-rich $Li_{1+x}M_{1-x}O_2$ electrodes (M = Mn, Ni, Co) for lithium batteries. Electrochem Commun 8:1531–1538

193. Deng H, Belharouak I, Yoon CS, Amine K (2010) High temperatura performance of surface-treated $Li_{1.1}(Ni_{0.15}Co_{0.1}Mn_{0.55})O_{1.95}$ layered oxide. J Electrochem Soc 157:A1035–A1039

194. Armstrong AR, Holzapfel M, Novák P, Johnson CS, Kang SH, Thackeray MM, Bruce PG (2006) Demonstrating oxygen loss and associated structural reorganization in the lithium battery cathode $Li[Ni_{0.2}Li_{0.2}Mn_{0.6}]O_2$. J Am Chem Soc 128:8694–8698

195. Yuan W, Zahng HZ, Liu Q, Li GR, Gao XP (2014) Surface modification of $Li(Li_{0.17}Ni_{0.2}Co_{0.05}Mn_{0.58})O_2$ with CeO_2 as cathode material for Li-ion batteries. Electrochim Acta 135:199–207

196. Wang ZQ, Chen YC, Ouyang CY (2015) Polaron states and migration in F-doped Li_2MnO_3. Phys Lett A 378:2449–2452

197. Röder P, Baba N, Wiemhöfer HD (2014) A detailed thermal study of a Li[Ni$_{0.33}$Co$_{0.33}$Mn$_{0.33}$]O$_2$-LiMn$_2$O$_4$-based lithium ion cell by accelerating rate and differential scanning calorimetry. J Power Sourc 248:978–987

198. Shi SJ, Tu JP, Tang YY, Liu XY, Zhao XY, Wang XL, Gu CD (2013) Morphology and electrochemical performance of Li[Li$_{0.2}$Mn$_{0.54}$Ni$_{0.13}$Co$_{0.13}$]O$_2$ cathode materials treated in molten salts. J Power Sourc 241:186–195

199. Toprakci O, Toprakci HAK, Li Y, Ji LW, Xue LG, Lee H, Zhang S, Zhang XW (2013) Synthesis and characterization of xLi$_2$MnO$_3 \cdot (1-x)$LiMn$_{1/3}$Ni$_{1/3}$Co$_{1/3}$O$_2$ composite cathode materials for rechargeable lithium-ion batteries. J Power Sourc 241:522–526

200. Shi SJ, Tu JP, Tang YY, Zhang YQ, Wang XL, Gu CD (2013) Preparation and characterization of macroporous Li$_{1.2}$Mn$_{0.54}$Ni$_{0.13}$Co$_{0.13}$O$_2$ cathode material for lithium-ion batteries via aerogel template. J Power Sourc 240:140–148

201. Zhenyao W, Biao L, Jin M, Dingguo X (2014) Molten salt synthesis and high-performance of nanocrystalline Li-rich cathode materials. RSC Adv 4:15825–15829

202. Zhang HZ, Qiao QQ, Li GR, Gao XP (2014) PO$_4^{3-}$ polyanion-doping for stabilizing Li-rich layered oxides as cathode materials for advanced lithium-ion batteries. J Mater Chem A 2:7454–7460

203. Myung ST, Lee KS, Sun YK, Yashiro H (2011) Development of high power lithium-ion batteries: layer Li[Ni$_{0.4}$Co$_{0.2}$Mn$_{0.4}$]O$_2$ and spinel Li[Li$_{0.1}$Al$_{0.05}$Mn$_{1.85}$]O$_4$. J Power Sources 196:7039–7043

204. Zhu Z, Zhu L (2014) Synthesis of layered cathode material 0.5Li$_2$MnO$_3$-0.5LiMn$_{1/3}$Ni$_{1/3}$Co$_{1/3}$O$_2$ by an improved co-precipitation method for lithium-ion battery. J Power Sourc 256:178–182

205. Shi SJ, Lou ZR, Xia TF, Gu CD, Tu JP (2014) Hollow Li$_{1.2}$Mn$_{0.5}$Co$_{0.25}$Ni$_{0.05}$O$_2$ microcube prepared by binary template method as a cathode material for lithium ion batteries. J Power Sourc 257:198–204

206. Croy KSH, Balasubramanian M, Thackeray MM (2011) Li$_2$MnO$_3$-based composite cathodes for lithium batteries: a novel synthesis approach and new structures. Electrochem Commun 13:1063–1066

207. Li J, Klöpsch R, Stan MC, Nowak S, Kunze M, Winter M, Passerini S (2011) Synthesis and electrochemical performance of the high voltage cathode material Li[Li$_{0.2}$Mn$_{0.56}$Ni$_{0.16}$Co$_{0.08}$]O$_2$ with improved rate capability. J Power Sourc 196:4821–4825

208. Chen Y, Xu G, Li J, Zhang Y, Chen Z, Kang F (2013) High capacity 0.5Li$_2$MnO$_3$-0.5LiNi$_{0.33}$Co$_{0.33}$Mn$_{0.33}$O$_2$ cathode material via a fast co-precipitation method. Electrochim Acta 87:686–892

209. Kim JH, Sun YK (2003) Electrochemical performance of Li[Li$_x$Ni$_{(1-3x)/2}$Mn$_{(1+x)/2}$]O$_2$ cathode materials synthesized by a sol-gel method. J Power Sourc 119:166–170

210. Zhao X, Cui Y, Xiao L, Liang H, Liu H (2011) Molten salt synthesis of Li$_{1+x}$(Ni$_{0.5}$Mn$_{0.5}$)$_{1-x}$O$_2$ as cathode material for Li-ion batteries. Solid State Ionics 192:321–325

211. Kim MG, Jo M, Hong YS, Cho J (2009) Template-free synthesis of Li[Ni$_{0.25}$Li$_{0.15}$Mn$_{0.6}$]O$_2$ nanowires for high performance lithium battery cathode. Chem Commun 218–220

212. Lu Z, MacNeil DD, Dahn JR (2001) Layered cathode materials Li[Ni$_x$Li$_{(1/3-2x/3)}$Mn$_{(1/3-x/3)}$]O$_2$ for lithium-ion batteries. Electrochem Solid State Lett 4:A191–A194

213. Wu Y, Manthiram A (2007) Effect of Al^{3+} and F$^-$ doping on the irreversible oxygen loss from layered Li[Li$_{0.17}$Mn$_{0.58}$Ni$_{0.25}$]O$_2$ cathodes. Electrochem Solid State Lett 10:A151–A154

214. Tran N, Croguennec L, Menetrier M, Weill F, Biensan P, Jordy C, Delmas C (2008) Mechanisms associated with the plateau observed at high voltage for the overlithiated Li$_{1.12}$(Ni$_{0.425}$Mn$_{0.425}$Co$_{0.15}$)$_{0.88}$O$_2$ system. Chem Mater 20:4815–4825

215. Wang ZY, Liu EZ, He CN, Shi CS, Li JJ, Zhao NQ (2013) Effect of amorphous FePO$_4$ coating on structure and electrochemical performance of Li$_{1.2}$Ni$_{0.13}$Co$_{0.13}$Mn$_{0.54}$O$_2$ cathode material for Li-ion batteries. J Power Sourc 236:25–32

216. Kang SH, Johnson CS, Vaughey JT, Amine K, Thackeray MM (2006) The effects of acid treatment on the electrochemical properties of $0.5Li_2MnO_3 \cdot 0.5LiNi_{0.44}Co_{0.25}Mn_{0.31}O_2$ electrodes in lithium cells. J Electrochem Soc 153:A1186–A1192

217. Tang JH, Wang ZX, Li XH, Peng WJ (2012) Preparation and electrochemical properties of Co-doped and none-doped $Li[Li_xMn_{0.65(1-x)}Ni_{0.35(1-x)}]O_2$ cathode materials for lithium batteries. J Power Sourc 204:187–192

218. Tran HY, Täubert C, Fleischhammer M, Axmann P, Küppers L, Wohlfahrt-Mehrens M (2011) $LiMn_2O_4$ spinel/$LiNi_{0.8}Co_{0.15}Al_{0.05}O_2$ blends as cathode materials for lithium-ion batteries. J Electrochem Soc 158:A556–A561

219. Gao J, Manthiram A (2009) Eliminating the irreversible capacity loss of high capacity layered $Li[Li_{0.2}Mn_{0.54}Ni_{0.13}Co_{0.13}]O_2$ cathode by blending with other lithium insertion hosts. J Power Sourc 191:644–647

220. Thackeray MM (1997) Manganese oxides for lithium batteries. Prog Solid State Chem 25:1–71

221. Gummow RJ, Liles DC, Thackeray MM (1993) Lithium extraction from orthorhombic lithium manganese oxide and the phase transformation to spinel. Mater Res Bull 28:1249–1256

222. Armstrong AR, Bruce PG (1996) Synthesis of layered $LiMnO_2$ as an electrode for rechargeable lithium batteries. Nature 381:499–500

223. Davidson IJ, McMillan RS, Murray JJ (1995) Rechargeable cathodes based on $Li_2Cr_xMn_{2-x}O_4$. J Power Sourc 54:205–208

224. Choi S, Manthiram A (2002) Factors influencing the layered to spinel-like phase transition in layered oxide cathodes. J Electrochem Soc 149:A1157–A1163

225. Doeff MM, Richardson TJ, Kepley L (1996) Lithium insertion processes of orthorhombic Na_xMnO_2-based electrode materials. J Electrochem Soc 143:2507–2516

226. Jeong YU, Manthiram A (1999) Synthesis and lithium intercalation properties of $Na_{0.5-x}Li_xMnO_{2+\delta}$ and $Na_{0.5-x}MnO_{2+\delta}$ cathodes. Electrochem Solid State Lett 2:421–424

227. Kim J, Manthiram A (1999) Amorphous manganese oxyiodides exhibiting high lithium intercalation capacity at higher current density. Electrochem Solid State Lett 2:55–57

228. Takeda Y, Kanno R, Tsuji Y, Yamamoto O (1983) Chromium oxides as cathodes for lithium cells. J Power Sourc 9:325–328

229. Yamamoto O, Takeda Y, Kanno R, Oyabe Y, Shinya Y (1987) Amorphous chromium oxide, a new lithium battery cathode. J Power Sourc 20:151–156

230. Kim J, Manthiram A (1997) Synthesis, characterization, and electrochemical properties of amorphous $CrO_{2-\delta}$ ($0 \leq \delta \leq 0.5$) cathodes. J Electrochem Soc 144:3077–3081

231. Abdel-Ghany AE, Mauger A, Groult H, Zaghib K, Julien CM (2012) Structural properties and electrochemistry of α-$LiFeO_2$. J Power Sourc 197:285–291

232. Wang W, Wang H, Liu S, Huang J (2010) Synthesis of γ-LiV_2O_5 nanorods as high-performance cathode for Li ion battery. J Solid State Electrochem 16:2555–2561

233. Yang G, Wang G, Hou W (2005) Microwave solid-state synthesis of LiV_3O_8 as cathode material for lithium batteries. J Phys Chem B 109:11186–11196

234. Delmas C, Braconnier JJ, Hagenmuller P (1982) A new variety of $LiCoO_2$ with an unusual packing obtained by exchange reaction. Mater Res Bull 17:117–123

235. Paulsen JM, Mueller-Neuhaus JM, Dahn JR (2000) Layered $LiCoO_2$ with a different oxygen stacking (O2 structure) as a cathode material for rechargeable lithium batteries. J Electrochem Soc 147:508–516